A&A 665, A126 (2022)
https://doi.org/10.1051/0004-6361/202244166

Astronomy & Astrophysics

PARSEC V2.0: Stellar tracks and isochrones of low- and intermediate-mass stars with rotation

C. T. Nguyen[1,3], G. Costa[2,3,4], L. Girardi[3], G. Volpato[2], A. Bressan[1], Y. Chen[5,6], P. Marigo[2], X. Fu[7,8,9,1], and P. Goudfrooij[10]

[1] SISSA, Via Bonomea 265, 34136 Trieste, Italy
e-mail: cnguyen@sissa.it
[2] Dipartimento di Fisica e Astronomia, Università degli studi di Padova, Vicolo Osservatorio 3, Padova, Italy
e-mail: guglielmo.costa@unipd.it
[3] INAF Osservatorio Astronomico di Padova, Vicolo dell'Osservatorio n. 5, Padova, Italy
[4] INFN – Padova, Via Marzolo 8, 35131 Padova, Italy
[5] Anhui University, Hefei 230601, PR China
[6] National Astronomical Observatories, Chinese Academy of Sciences, Beijing 100101, PR China
[7] Purple Mountain Observatory, Chinese Academy of Sciences, Nanjing 210023, PR China
[8] The Kavli Institute for Astronomy and Astrophysics at Peking University, 100871 Beijing, PR China
[9] INAF Osservatorio di Astrofisica e Fisica dello Spazio, Via Gobetti 93/3, 40129 Bologna, Italy
[10] Space Telescope Science Institute, 3700 San Martin Drive, Baltimore, MD 21218, USA

Received 1 June 2022 / Accepted 19 July 2022

ABSTRACT

We present a new comprehensive collection of stellar evolutionary tracks and isochrones for rotating low- and intermediate-mass stars assembled with the updated version of PARSEC V2.0. This version includes our recent calibration of the extra mixing from overshooting and rotation, as well as several improvements regarding the nuclear reaction network, treatment of convective zones, mass loss, and other physical input parameters. The initial mass of the stellar models covers the range 0.09 $M_\odot$ to 14 $M_\odot$ for six sets of initial metallicity, from $Z = 0.004$ to $Z = 0.017$. Rotation is considered for stars above ∼1 $M_\odot$ with a smooth transition between non-rotating and extremely fast-rotating models, based on the initial mass. For stars more massive than ∼1.3 $M_\odot$, the full rotation range, from low to critical, is considered. We adopt the solar-scaled chemical mixtures with $Z_\odot = 0.01524$. All the evolutionary phases from the pre-main-sequence to the first few thermal pulses on the asymptotic giant branch or central C exhaustion are considered. The corresponding theoretical isochrones are further derived with TRILEGAL code and are converted into several photometric systems, taking different inclination angles into account. Besides magnitudes, they also offer many other stellar observables in line with the data being provided by current large surveys. The new collection is fully integrated in a user-friendly web-interface for the benefit of easily performing stellar population studies.

Key words. stars: evolution – stars: rotation – Hertzsprung-Russell and C-M diagrams – stars: low-mass

1. Introduction

The PAdova and tRieste Stellar Evolutionary Code (PARSEC) was first implemented in Bressan et al. (2012) and then used in several works aimed at producing large grids of stellar evolutionary tracks and isochrones. For instance, Chen et al. (2014) extended the calculation to very low-mass star (VLMS) models, Tang et al. (2014) and Chen et al. (2015) pursued massive stars up to 350 $M_\odot$, and Fu et al. (2018) studied the evolution with α-enhanced compositions. Extended sets of isochrones using PARSEC tracks were described in Bressan et al. (2012) and Marigo et al. (2017). More recently, a significant development was presented in Costa et al. (2019a), who included the effects of rotation in the new version of the code, PARSEC V2.0[1].

As described in von Zeipel (1924a,b), Kippenhahn et al. (1970), Zahn (1992), Meynet & Maeder (1997), and Chieffi & Limongi (2013, 2017), rotation might have a significant impact on the stellar structure induced by geometrical distortion, extra mixing, and enhanced mass-loss rates. Observational evidence regarding the large fractions of rapidly rotating stars among the Milky Way field stars (e.g. Royer et al. 2007) and in star clusters in Magellanic Clouds (e.g. Dupree et al. 2017; D'Antona et al. 2017) suggests that rotation may indeed become an important driving agent for stellar evolution. Furthermore, it may be concurrent with other physical processes that drive extra mixing, such as convective overshooting (see e.g. Jermyn et al. 2018; Costa et al. 2019a). The effect of extra mixing caused by overshooting from the unstable core was introduced a few decades ago (e.g. Saslaw & Schwarzschild 1965; Maeder 1975; Roxburgh 1978; Bressan et al. 1981, 1986, 1993; Bertelli et al. 1984, 1990; Meynet et al. 1994; Fagotto et al. 1994a,b; Girardi et al. 2000) and is now incorporated into most libraries of stellar evolutionary tracks (e.g. Demarque et al. 2004; Pietrinferni et al. 2004; Weiss & Schlattl 2008; Paxton et al. 2011, 2018; Mowlavi et al. 2012; Bressan et al. 2012; Bossini et al. 2015; Spada et al. 2017; Hidalgo et al. 2018). Many authors also suggest a variation in

[1] Stellar tracks and isochrones computed in this work are available at the following links: http://stev.oapd.inaf.it/PARSEC and http://stev.oapd.inaf.it/cmd, respectively.

the overshooting efficiency, usually parameterised by the efficiency parameter λ_{ov}, with the initial mass (see e.g. Pols et al. 1998). Analysis of double-lined eclipsing binaries (DLEBs; Claret & Torres 2016, 2017, 2018, 2019) supports a growing efficiency in the mass range $\sim$1−1.7 $M_{\odot}$ with a plateau in λ_{ov} above this range. However, the best fits of the DLEB parameters require a certain degree of stochasticity in some other important parameters, such as the mixing length scale, which in our opinion is difficult to accept, particularly in the case of binary components with the same mass. Indeed, Costa et al. (2019a) show that the observations of DLEBs could be well explained by the interplay between a 'fixed' overshooting efficiency and a varying initial rotational velocity. In fact, the latter also depends on environmental conditions. The results obtained by Costa et al. (2019a) can thus be considered an important step in the calibration of the efficiency of the overshooting phenomenon, at least in the domain of low- and intermediate-mass stars (IMSs). This calibration has been subsequently supported by a combined analysis of Cepheids in the Large Magellanic Cloud (LMC) star cluster NGC 1866 and the colour-magnitude diagrams (CMDs) of its multiple stellar populations (Costa et al. 2019b).

Following these initial tests performed with the new code, we present in this paper the new sets of evolutionary tracks and the corresponding isochrones for the PARSEC models with rotation. The initial mass range presented in this paper goes from 0.09 $M_{\odot}$ to 14 $M_{\odot}$. Models of more massive stars have already been computed for some particular purposes (Spera et al. 2019; Costa et al. 2021, 2022), but the full set including rotation is still in preparation and will be presented in a dedicated paper.

All the tracks start at the pre-main-sequence (PMS) phase and are terminated at a stage that depends on the initial mass: at ages largely exceeding the Hubble time; at the initial stages of the thermally pulsing asymptotic giant branch (TP-AGB); or at carbon exhaustion for more massive stars. The tracks are computed with an initial metal content ranging from $Z = 0.004$ to 0.017 and with an initial He mass fraction that follows a linear enrichment law (Bressan et al. 2012). Tracks at lower metallicity are computed with an enhanced partition, and the details of these models with rotation will be presented in an upcoming paper. For every metallicity, we consider initial rotation rates from zero to the critical value. The theoretical isochrones are then derived and converted into several photometric systems.

The structure of this paper is as follows. In Sect. 2 we review the main input physics used in the present calculations. We pay particular attention to differences with respect to the previous non-rotating models in the event of important physical input changes. In Sect. 3 we describe the effects of rotational mixing on the evolution of our stellar models. We also compare our current models with previous non-rotating ones and perform some comparisons with existing models in the literature. The corresponding isochrones and the quantities provided are described in detail in Sect. 4. Finally, in Sect. 5 we show a few preliminary fits to the observed CMDs of the two open clusters M 67 and NGC 6633, and draw our main conclusions.

2. Input physics

The input physics used in PARSEC is described in Bressan et al. (2012), Tang et al. (2014), Chen et al. (2014), Fu et al. (2018), and Costa et al. (2019a,b). Here, we briefly summarise the main points that are more important for the low-mass stars (LMSs) and IMSs dealt with in this paper.

2.1. Solar metallicity, opacities, nuclear reactions, mixing length, equation of state

The abundance of elements heavier than ^{4}He in the Sun is still uncertain. The early compilation by Grevesse & Sauval (1998), consisting of the abundances of 90 elements from lithium to uranium, yielded the solar metallicity $Z_{\odot} = 0.017$. Later, Asplund et al. (2006, 2009) claimed lower values, $Z_{\odot} = 0.0122$ and $Z_{\odot} = 0.0134$, respectively, or Lodders et al. (2009) with $Z_{\odot} = 0.0141$. Recent solar wind measurements give $Z_{\odot} = 0.0196 \pm 0.0014$ (von Steiger & Zurbuchen 2016). In this paper, we adopt the solar-scaled mixtures by Caffau et al. (2011) where the current solar metallicity is $Z_{\odot} = 0.01524$, which is an intermediate value between those preferred by Asplund et al. (2009) and von Steiger & Zurbuchen (2016). Further extensions to other metallicity ranges with more suitable input physics, for example α-enhanced mixtures, will be provided in the forthcoming works.

The Rosseland mean opacities, κ_{rad}, are the same as those of PARSEC V1.2S. In the high temperature regime, $4.2 \leq \log(T/K) \leq 8.7$, the opacity tables are provided by the Opacity Project At Livermore (OPAL; see Iglesias & Rogers 1996), while in the low temperature regime $3.2 \leq \log(T/K) \leq 4.1$ we generate the opacity tables with the AESOPUS tool (see Marigo & Aringer 2009, for details). In the transition region $4.1 \leq \log(T/K) \leq 4.2$, the opacities are linearly interpolated between the OPAL and AESOPUS values. The contribution from conduction is computed following Itoh et al. (2008).

The transport of convective energy is described by the mixing length theory of Böhm (1958), adopting the value of mixing-length parameter $\alpha_{MLT} = 1.74$ calibrated on the solar model by Bressan et al. (2012; see also Sonoi et al. 2019 for more calibrations). It is interesting, however, to note that the variation in α_{MLT} for different stars has recently been remarked upon; for example, Viani et al. (2018) suggest a dependence of $\alpha_{MLT}/\alpha_{MLT\odot}$ on gravity, effective temperature and metallicity, while the study of Song et al. (2020) in FGK stars mainly focuses on the impact from metallicity. While these recent studies might be an inspiration for future works, at the moment we use the solar mixing-length parameter for all calculations, $\alpha_{MLT} = \alpha_{MLT\odot} = 1.74$. The equation of state in PARSEC V2.0 is computed with the freely available FREEEOS code developed by A. W. Irwin[2].

The nuclear reaction network, after the updates by Fu et al. (2018) and Costa et al. (2021), includes the p-p chains, the CNO tri-cycle, the Ne-Na and Mg-Al chains, ^{12}C, ^{16}O and ^{20}Ne burning reactions, and the α-capture reactions up to ^{56}Ni, for a total of 72 different reactions tracing 32 isotopes: ^{1}H, D, ^{3}He, ^{4}He, ^{7}Li, ^{7}Be, ^{12}C, ^{13}C, ^{14}N, ^{15}N, ^{16}O, ^{17}O, ^{18}O, ^{19}F, ^{20}Ne, ^{21}Ne, ^{22}Ne, ^{23}Na, ^{24}Mg, ^{25}Mg, ^{26}Mg, ^{26}Al, ^{27}Al, ^{28}Si, ^{32}S ,^{36}Ar, ^{40}Ca, ^{44}Ti, ^{48}Cr, ^{52}Fe, ^{56}Ni, and ^{60}Zn. We note that in the present calculations we do not go beyond the central carbon burning (but see Costa et al. 2021, for massive stars).

2.2. Convective overshooting

Core overshooting (COV): The convective unstable region is well defined within the framework of the Schwarzschild criterion (Schwarzschild 1958). However, in reality, the convective elements can travel up to a certain point beyond the border of the unstable region until their velocity drops to zero. This phenomenon is called overshooting. The determination of the edge of the true convective core was described in Bressan et al. (1981).

[2] http://freeeos.sourceforge.net/

Table 1. Values of core and EOV parameters, λ_{ov} and Λ_e/H_P, respectively, which correspond to each initial mass, $M_i/M_\odot$, in six metallicities (Zs).

λ_{ov}	Λ_e/H_P	$Z = 0.017$ $M_i/M_\odot$	$Z = 0.014$ $M_i/M_\odot$	$Z = 0.01$ $M_i/M_\odot$	$Z = 0.008$ $M_i/M_\odot$	$Z = 0.006$ $M_i/M_\odot$	$Z = 0.004$ $M_i/M_\odot$	Note
0.000	0.000	<0.80	<0.80	<0.75	<0.75	<0.70	<0.70	M_{vlm}
0.000	0.500	<1.18	<1.16	<1.14	<1.14	<1.09	<1.06	
0.000	0.500	1.18	1.16	1.14	1.14	1.09	1.06	M_{O1}
0.027	0.513	1.20	1.18	1.16	1.16	1.11	1.08	
0.053	0.527	1.22	1.20	1.18	1.18	1.13	1.10	
0.080	0.540	1.24	1.22	1.20	1.20	1.15	1.12	
0.107	0.553	1.26	1.24	1.22	1.22	1.17	1.14	
0.133	0.567	1.28	1.26	1.24	1.24	1.19	1.16	
0.160	0.580	1.30	1.28	1.26	1.26	1.21	1.18	
0.187	0.593	1.32	1.30	1.28	1.28	1.23	1.20	
0.213	0.607	1.34	1.32	1.30	1.30	1.25	1.22	
0.240	0.620	1.36	1.34	1.32	1.32	1.27	1.24	
0.267	0.633	1.38	1.36	1.34	1.34	1.29	1.26	
0.293	0.647	1.40	1.38	1.36	1.36	1.31	1.28	
0.320	0.660	1.42	1.40	1.38	1.38	1.33	1.30	
0.347	0.673	1.44	1.42	1.40	1.40	1.35	1.32	
0.373	0.687	1.46	1.44	1.42	1.42	1.37	1.34	
0.400	0.700	1.48	1.46	1.44	1.44	1.39	1.36	M_{O2}
0.400	0.700	>1.48	>1.46	>1.44	>1.44	>1.39	>1.36	

Notes. The value of the transition masses, M_{vlm}, M_{O1}, and M_{O2}, of each metallicity is also noted.

In PARSEC, the overshooting parameter (λ_{ov}) is taken across the unstable border; therefore, the COV length is $l_{ov} \sim \frac{1}{2}\lambda_{ov}H_P$, where H_P is the local pressure scale height.

Envelope overshooting (EOV): the overshooting downwards from the base of the convective envelope has been invoked to explain the observations of the location of the red-giant-branch bump (RGBB) or the extension of blue loops in the CMD (Alongi et al. 1991; Cassisi et al. 2002; Tang et al. 2014; Fu et al. 2018). Solar calibration with helioseismic data have been done by Christensen-Dalsgaard et al. (2011).

In PARSEC models, the treatment of overshoot from both the convective core and envelope are related to the initial masses. For this reason, we describe the values of overshooting parameters that we use in our calculations more completely in the next subsection.

2.3. Mass range for core and envelope overshooting

In a narrow interval of masses around 1 $M_\odot$, there is the transition between stars that burn central hydrogen in a radiative core and those that burn hydrogen in a convective core due to the predominance of the CNO-cycle over the pp-cycle. Assessing the efficiency of COV in this mass range is a particularly delicate matter both theoretically (e.g. Bertelli et al. 1986, 1990; Aparicio et al. 1990; Ventura et al. 1998; Mowlavi et al. 2012; Higl et al. 2021) and observationally (e.g. Torres et al. 2014; Claret & Torres 2016, 2018; Noll et al. 2021). This happens because the inclusion of overshooting modifies the structure and the following evolution of the stars in an irreversible way. In fact, the smallest stars in this mass range reach the zero-age main sequence (ZAMS) with small convective cores that disappear as the central H-burning proceeds. If we apply an efficient overshooting to these models, the convective cores do not disappear, but instead tend to become larger and larger, producing a significantly different evolution. To avoid this behaviour, which is not favoured by observations (Costa et al. 2019a; Girardi et al. 2000), we define the limiting mass M_{O1} as the largest initial mass of a star showing a vanishing convective core during the early hydrogen burning phase, calculated without overshooting. This mass depends on the initial chemical composition adopted. On the other hand, slightly above this mass limit, observations favour an already well-developed overshooting efficiency, with $\lambda_{ov} = \lambda_{ov,max}$. This second mass limit is defined as $M_{O2} = M_{O1} + 0.3\ M_\odot$.

In PARSEC v2.0, we define an initial mass range where the transition from models with a radiative core to models with a fully grown convective core takes place, $M_{O1} \leq M_i \leq M_{O2}$. For initial masses M_i below M_{O1}, the core is stable against convection and energy is transported by radiation. For M_i between M_{O1} and M_{O2}, the overshooting parameter is let to increase linearly from $\lambda_{ov} = 0$ up to a maximum value $\lambda_{ov,max}$, in order to have a smooth transition in the properties of the stars. For $M_i \geq M_{O2}$, the overshoot is applied with its maximum efficiency, $\lambda_{ov} = \lambda_{ov,max} = 0.4$ following Costa et al. (2019a). This value corresponds to an overshooting length, l_{ov}, which extends about $0.2\ H_P$ above the Schwarzschild border.

In this paper we decided to switch on the EOV for LMSs and IMSs only. For stars with mass $M_i < M_{O1}$, we adopted $\Lambda_e = 0.5\ H_P$, as inspired by Fu et al. (2018); for stars with mass $M_i > M_{O2}$, we applied the maximum efficiency, as we did for COV; therefore, $\Lambda_e = 0.7\ H_P$, as used in Alongi et al. (1991) and Bressan et al. (2012). In the transition region, Λ_e of a star is linearly interpolated between $0.5\ H_P$ and $0.7\ H_P$. Table 1 shows the values of λ_{ov} and Λ_e adopted for each initial mass.

2.4. Rotation

We used PARSEC v2.0 to compute evolutionary tracks of rotating low- and IMSs. The code uses the methodology developed by Kippenhahn & Thomas (1970) and Meynet & Maeder (1997), implemented and described in Costa et al. (2019a,b). The basic quantity describing the effect of rotation in the stellar structure

is the angular rotation rate, ω, defined as

$$\omega = \frac{\Omega}{\Omega_c}, \quad \Omega_c = \left(\frac{2}{3}\right)^{3/2} \sqrt{\frac{GM}{R_{pol}^3}}, \tag{1}$$

where Ω is the angular velocity, Ω_c is the critical angular velocity (or breakup velocity), that is, the angular velocity at which the centrifugal force is equal to the effective gravity at the equator. G is the gravitational constant, M is the mass enclosed by R_{pol} that is the polar radius.

We considered a wide range of initial rotation rates, from non-rotating models ($\omega_i = 0$) to models initially very near the critical breakup rotational velocity ($\omega_i = 0.99$). It is commonly accepted that LMSs do not reach high values of the rotational speed, compared to intermediate and high-mass stars. McQuillan et al. (2014) reports a sample of the rotation period of more than 34 000 main-sequence (MS) stars. In their Fig. 1, there is a clear trend for larger periods in smaller masses. This trend inevitably implies that stars with lower masses have lower initial rotational speeds.

On the other hand, rotation may reach high initial values for masses where convection is well developed (Costa et al. 2019a). For this reason, in analogy to what we did for the efficiency of convective COV, rotation was not considered for $M_i \leq M_{O1}$ while, for $M_i \geq M_{O2}$, models were computed for the following initial rotation rates: $\omega_i = 0.0, 0.30, 0.60, 0.80, 0.90, 0.95, 0.99$. For stars with an initial mass in the range $M_{O1} \leq M_i < M_{O2}$ we computed models with an initial rotation rate up to a maximum value of

$$\omega_{i,max}(M) \equiv 0.99 \left(\frac{M - M_{O1}}{M_{O2} - M_{O1}}\right). \tag{2}$$

It is also important to mention that, in this version, the rotation is switched on a few models before the ZAMS phase. At this stage, the code computes the angular velocity Ω that corresponds to the initial rotation rate ω_i and assigns it to each shell of the star, forcing a solid body rotation. From the ZAMS on, the solid body rotation constraint is relaxed, and the stellar rotation evolves accordingly with the conservation and the transport of angular momentum.

2.5. Transport of angular momentum and chemical mixing

The transport of angular momentum is treated based on the pure diffusive approximation (Heger et al. 2000), where the total diffusion coefficient comes from three components,

$$D = D_{mix} + D_{s.i.} + D_{m.c.}, \tag{3}$$

where D_{mix} is the diffusion coefficient in the convective zones. The last two terms are related to the shear instability and the meridional circulation. To compute the diffusion coefficient of the shear instability, we use the formula by Talon & Zahn (1997), which reads

$$D_{s.i.} = \frac{8}{5} \frac{Ri_c (r d\Omega_r/dr)^2}{N_T^2/(K + D_h) + N_\mu^2/D_h}, \tag{4}$$

where the Brunt–Väisälä frequency is split into N_T^2 and N_μ^2, $Ri_c = 1/4$ is the critical Richardson number, K is the thermal diffusivity, and D_h is the coefficient of horizontal turbulence.

When angular momentum transport is treated with the diffusive approach, the diffusion coefficient for the meridional circulation remains to be defined. Some authors define it as the product of circulation velocity and its typical length scale (Heger et al. 2000), while others use the same coefficient provided for chemical transport (Chieffi & Limongi 2013). For the sake of simplicity, we decided to follow the latter approach. Therefore, we adopt the coefficient by Chaboyer & Zahn (1992), which reads

$$D_{m.c.} \simeq \frac{|rU|^2}{30 D_h}, \tag{5}$$

where U is the radial component of the meridional circulation velocity (see also Maeder 2009; Potter et al. 2012). It should be noted that, as discussed by Chaboyer & Zahn (1992) and Zahn (1992), this coefficient takes into account the net effect of the meridional current and horizontal diffusion for chemical species. A more detailed description of angular momentum transport should include meridional circulation as an advective process. However, due to the difficult numerical implementation of the advective-diffusive treatment, and the fact that the angular momentum redistribution goes in the direction of flattening ω profiles during the MS phase (Chieffi & Limongi 2013), we decided to use the simpler diffusive approach.

Future PARSEC versions will include the full advective-diffusive treatment for angular momentum transport. We refer to Costa et al. (2019a) for more details on the numerical implementation of rotation.

Another important difference of this new version, PARSEC v2.0, with respect to PARSEC v1.2S concerns chemical mixing. While in the latter version the gas was chemically homogenised within convective regions, in the present version we adopt a diffusive approach and solve a unique equation for chemical variation due to nuclear reactions, turbulent motions, molecular diffusion, and rotational mixing. The turbulent diffusion coefficient is calculated with the usual approximation $D_T = \frac{1}{3} v_c l_c$ where the velocity of the eddies, v_c, and their mean free path, l_c are obtained from the mixing length theory (Böhm-Vitense 1958).

We note that, while all the above processes can be treated at once, molecular diffusion can be switched off in models where the COV reaches its maximum efficiency (above $M \geq M_{O2}$), because, in such models, the effects of molecular diffusion become negligible with respect to turbulent diffusion and, eventually, rotational mixing. This allows a speed-up of the calculations without loss of generality. We discuss the effects brought by adopting either of the aforementioned mixing schemes later on.

2.6. Mass-loss rates

The effects of mass loss in the evolution of low and IMSs have been extensively studied in many papers (e.g. Reimers 1975; Bloecker 1995; Schröder & Cuntz 2005; Cranmer & Saar 2011; Rosenfield et al. 2014; Kalirai et al. 2008; Catalán et al. 2008; Salaris et al. 2009). In PARSEC models, as well as in previous models of the same group (Girardi et al. 2000; Bertelli et al. 2008), mass loss was not activated in the calculations of the low-mass tracks but only at the stage of isochrone calculations. This approximation has been tested in many different applications and has always been considered acceptable from our group. It derives from the fact that the red-giant-branch (RGB) evolution of LMSs is just marginally affected by this process, which eventually becomes important only very near to the tip of the red-giant branch (TRGB). Therefore, mass loss just causes a decrease in mass between the RGB and the 'zero-age horizontal branch' (ZAHB) stage. This decrease was easily taken into

account when interpolating the helium-burning tracks to prepare isochrones. This method allows a great flexibility (different mass-loss prescriptions can be tested without recomputing the evolutionary tracks) and speed-up at the level of isochrone calculation. In the more advanced phases of low and IMSs, typically from the early up to the end of the TP-AGB phase, mass-loss is one of the main processes driving the evolution and cannot be neglected. However, the evolution of stars in these phases is computed subsequently with the COLIBRI code (Marigo et al. 2013), where the most updated mass-loss rates are implemented.

With the inclusion of rotation, mass-loss cannot be decoupled from evolution anymore and must be included in all evolutionary phases. This is because rotation may enhance the mass loss, affecting the evolutionary path of the star. This may become dramatic when the star is in proximity to the critical breakup velocity.

In this paper, we apply the Reimers (1975, 1977) law for non-rotating LMSs, which is

$$\dot{M}(\omega = 0) = \eta \times 1.343 \times 10^{-5} \frac{L^{1.5}}{m T_{\rm eff}^2}, \quad (6)$$

where $\dot{M}$ is the mass-loss rate in $M_\odot$/yr, L and m are the luminosity and mass in solar units, respectively, and $T_{\rm eff}$ is the effective temperature in K. The η is an efficiency coefficient that is generally calibrated against CMDs of globular clusters, as for instance in Renzini & Fusi Pecci (1988) where the derived η is 0.35, or Aaronson & Mould (1982) who claimed that η = 0.5−0.7 fits well their data of the red globular clusters in the Magellanic Clouds. In this paper, we adopt η = 0.2, as more recently indicated from the asteroseismic analysis of the two old open clusters NGC 6791 and NGC 6819 by Miglio et al. (2012). As described in Chen et al. (2015), for non rotating intermediate-mass and massive stars we adopt the mass-loss rate from de Jager et al. (1988) and Vink et al. (2001), respectively, both corrected by a factor that assumes the same dependence on the surface metallicity (i.e. $\dot{M} \propto (Z/Z_\odot)^{0.85}\, M_\odot$/yr).

In the case of rotating stars, the mass-loss rates are enhanced by a factor that depends on the surface tangential velocity, v, as expressed in Costa et al. (2019a,b). By numerically solving the fluid equations of a radiation-stellar wind model, Friend & Abbott (1986) yield a relation where the mass-loss rate of a rotating star is modified by a factor with respect to the mass loss of a non-rotating model, which is

$$\dot{M}(\omega) = \dot{M}(\omega = 0) \left(1 - \frac{v}{v_{\rm crit}}\right)^{-\xi}, \quad (7)$$

where ξ = 0.43 is provided in Bjorkman & Cassinelli (1993) by fitting the numerical result of Friend & Abbott (1986). $\dot{M}(\omega = 0)$ is the mass-loss rate in case of zero rotation and $v_{\rm crit}$ is the surface critical velocity, which is usually defined as (Heger et al. 2000)

$$v_{\rm crit}^2 = \frac{Gm}{r}(1 - \Gamma_{\rm e}), \quad (8)$$

where G, m, and r are the gravitational constant, mass, and radius in solar units, respectively, and $\Gamma_{\rm e}$ is the Eddington factor. In this paper, the dependence of $\Gamma_{\rm e}$ with the angular velocity is neglected, instead, it should be considered for angular velocities near the critical one (Maeder & Meynet 2000).

3. Evolutionary tracks

Before going into more detail on the analysis of our stellar evolutionary tracks, we summarise some of the main points on the adopted input physics. Firstly, we computed models with six initial metallicities: Z = 0.004, 0.006, 0.008, 0.01, 0.014, 0.017, which are relevant for the study of young and intermediate-age star clusters in the Milky Way disc and in the Magellanic Clouds. The initial helium mass fraction follows the enrichment law: $Y = Y_{\rm p} + \frac{\Delta Y}{\Delta Z} Z$, where $Y_{\rm p}$ = 0.2485 is the primordial He abundance (Komatsu et al. 2011); the helium-to-metal enrichment ratio $\Delta Y/\Delta Z$ = 1.78 is based on the solar calibration in Bressan et al. (2012). More specifically, the corresponding initial He mass fraction is Y = 0.256, 0.259, 0.263, 0.267, 0.273, 0.279; and the initial hydrogen abundance X = 0.740, 0.735, 0.729, 0.723, 0.713, 0.704.

Second, the initial rotation rate is parameterised by $\omega_{\rm i}$: for each set of metallicity above, we compute models with rotation rates going from zero to very near the critical point, $\omega_{\rm i}$ = 0.00, 0.30, 0.60, 0.80, 0.90, 0.95, 0.99. The treatment of rotation rate for each single star in terms of mass is described in Sect. 2.4.

Third, the convective overshoot: we apply the overshoot from both the convective core and envelope in the calculations as described in Sects. 2.2 and 2.3.

Lastly, the mass intervals: For convenience, we describe the evolutionary tracks in three mass ranges: (i) VLMSs have initial masses $M_{\rm i} \lesssim M_{\rm vlm}$, where $M_{\rm vlm}$ is the smallest initial mass of a star that is able to ignite helium within the Hubble timescale. Stars with mass smaller than this limit spend their lifetime mainly on the hydrogen-burning phase; (ii) LMSs have initial masses between $M_{\rm vlm}$ and $M_{\rm HeF}$, which includes $M_{\rm O1}$ and $M_{\rm O2}$ as mentioned above; and (iii) IMSs with $M_{\rm i} > M_{\rm HeF}$. $M_{\rm HeF}$ is defined as the transition mass between stars that develop an electron-degenerate core after the MS and hence develop an extended RGB with an He flash at its tip, and those that do not, hence quietly initiating He-core burning in a non-degenerate core.

Figure 1 shows the dependence of $M_{\rm O1}$, $M_{\rm O2}$ and $M_{\rm HeF}$ as a function of metallicity, for non-rotating models. We also draw the six metallicities computed in this project. Table 1 lists the values of $\lambda_{\rm ov}$ and $\Lambda_{\rm e}$ adopted for each initial mass. Finally, the database of all stellar evolutionary tracks that we produced in this work is available online[3].

3.1. Very low-mass stars

The PARSEC models for VLMSs ($0.09\,M_\odot \leq M_{\rm i} \lesssim M_{\rm vlm}$) were described in Chen et al. (2014) and successfully calibrated against the mass-radius relation of a sample of eclipsing binaries. For this purpose, the authors slightly modified the $T-\tau$ relations provided by PHOENIX (BT-Settl) atmosphere models (see Asplund et al. 2009; Allard et al. 2012). After this calibration, the corresponding isochrones were able to reproduce well the very low ZAMS of old globular clusters NGC 6397 and 47 Tuc, and of the open clusters M 67 and Praesepe. These models were also adopted to fit *Gaia* DR2 CMD diagrams (Gaia Collaboration 2018a). Here, we continue to use these very low-mass evolutionary tracks, referring to Chen et al. (2014) for all details.

3.2. Low-mass stars

3.2.1. From the pre-main-sequence to the tip of the RGB

We computed models of LMSs with initial masses in the interval from $M_{\rm vlm}$ to $M_{\rm HeF}$. The mass step is 0.05 $M_\odot$ in the mass range

[3] http://stev.oapd.inaf.it/PARSEC

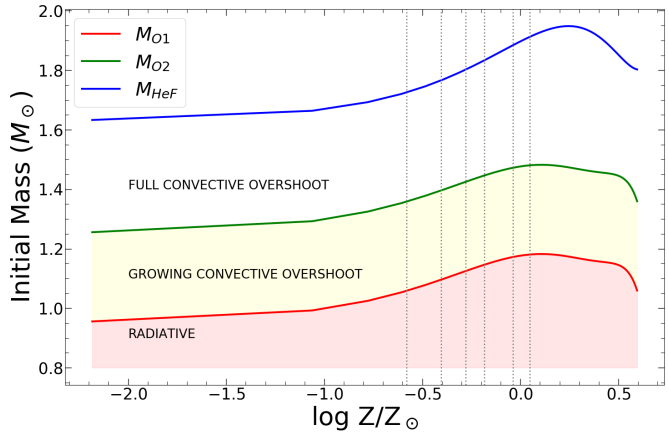

Fig. 1. Transition masses (M_{O1}, M_{O2}, M_{HeF}) as a function of metallicity in the case of no rotation. The red and green lines indicate M_{O1} and M_{O2}, respectively; the blue line indicates M_{HeF}. The red area indicates models with a radiative core without convective overshooting. The yellow area delineates the region of growing overshooting efficiency, while full overshooting efficiency occurs in the region above the green line. The vertical dotted grey lines mark the six computed initial metallicities. The solar metallicity is $Z_\odot = 0.01524$, from Caffau et al. (2011).

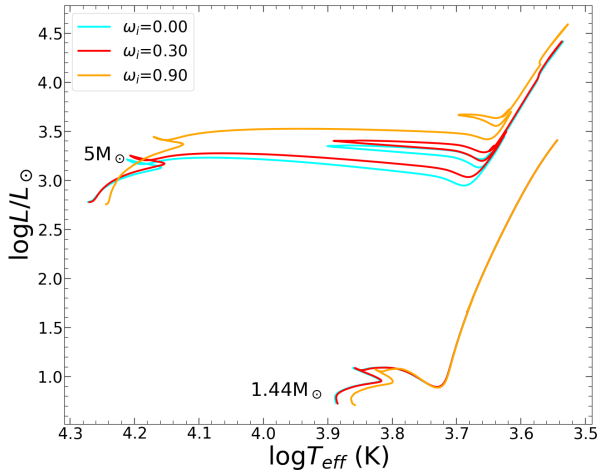

Fig. 2. HRD of stars with initial masses of 1.44 $M_\odot$ and 5 $M_\odot$ with the composition $Z = 0.008$, $Y = 0.263$ for initial rotation rates $\omega_i = 0.00$, 0.30, and 0.90 (cyan, red, and orange lines, respectively). We do not plot the evolution on the PMS phase, for sake of clarity.

from M_{vlm} to 0.8 $M_\odot$, 0.02 $M_\odot$ for the range from 0.8 $M_\odot$ to M_{O2}, and 0.1 $M_\odot$ for masses above M_{O2}. All the LMSs tracks begin from the PMS phase and end at the TRGB, where the star ignites its central He under strongly degenerate conditions (the so-called He flash).

Figure 2 shows the Hertzsprung-Russell diagram (HRD) of 1.44 $M_\odot$ stars with different initial rotation rates. It should be noted that, for rotating stars, T_{eff} is actually an average value over the isobaric surface; more precisely it is the value that a non-rotating star with the same 'volumetric radius' would have to produce the same total luminosity. The volumetric radius is defined as the radius of a sphere with the same volume as that of the rotating star. The local effective temperature characterising different points at the surface of the star, instead, is a quantity that varies along the co-latitude angle ($\theta = 0°$ aligns with the rotation axis), becoming cooler towards the equator. This can be explained by the proportionality between T_{eff}^4 and

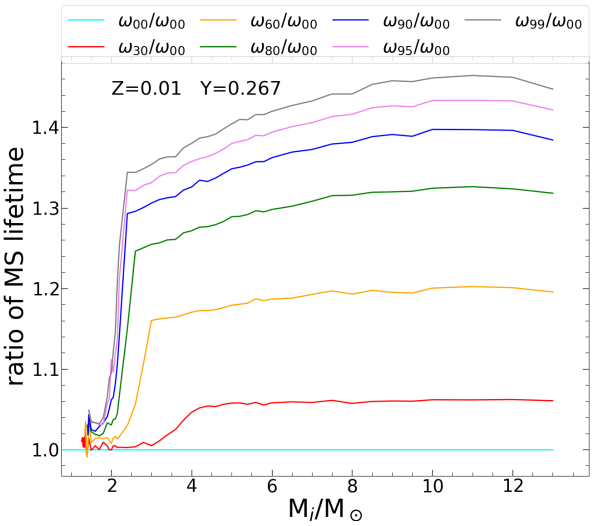

Fig. 3. Ratio between the MS lifetimes of rotating and non-rotating models of the same mass, as a function of initial mass in the set $Z = 0.01$, $Y = 0.267$. This lifetime is measured from the ZAMS until the exhaustion of the central H ($X_c < 10^{-5}$). Different values of ω_i, from 0 to 0.99, are considered, as indicated in the legend.

effective gravity g_{eff}, based on von Zeipel's theorem (von Zeipel 1924b; Espinosa Lara & Rieutord 2007). In turn, the local effective gravity is reduced by the centrifugal force, which is higher for a higher rotation rate. Therefore, as we see in Fig. 2, the higher the rotation rate, the cooler the star is (by means of the average value) during the MS. In the post-MS phases, the conservation of angular momentum forces the surface angular velocity to drop down when the star expands, hence causing the star to evolve along the same path of non-rotating stars.

Another effect of rotation is that the faster the stars rotate, the longer they stay in the MS phase (Eggenberger et al. 2010; Ekström et al. 2012; Costa et al. 2019b). Figure 3 shows the ratio of the MS duration between models with different ω_i and their standard non-rotating counterparts, $\omega_i = 0$, as a function of the initial mass M_i and for $Z = 0.01$. We see that this ratio is higher than 1 for all rotating models and becomes higher as ω_i increases. In the low-mass range ($M \lesssim 1.8\,M_\odot$) the ratio remains modest, while it increases significantly in the domain of intermediate-mass and massive stars. This is understandable because of the lower efficiency of rotational mixing in LMSs with respect to intermediate and massive ones, as will be discussed later in Sect. 3.3.

We also find that in the low-mass range, the size of the convective core does not depend significantly on ω_i. This can be seen in Fig. 4 for the models of $M_i = 1.44\,M_\odot$ and $Z = 0.017$.

After the formation of the H-exhausted core, the star enters into the sub-giant phase and then ascends the RGB. Expansion of the envelope leads to a decrease in surface rotation velocity. This impact is illustrated in Fig. 5, where the equatorial tangential velocity drastically decreases after leaving the MS. The drop down on rotation rate results in an evolution as a non-rotating star, as already mentioned and as illustrated in the HRD of Fig. 2. We found that the luminosity at the TRGB phase is almost the same for any applied rotational rates (see also Ekström et al. 2012; Georgy et al. 2013).

For instance, the TRGB luminosity of the $Z = 0.004$, $M_i = 1.36\,M_\odot$ star is $\log L/L_\odot = 3.38771$, 3.38934 and 3.38919 for the models with $\omega_i = 0.00$, 0.60 and 0.90, respectively. We see that the difference is less than 0.0016 dex in any case, and

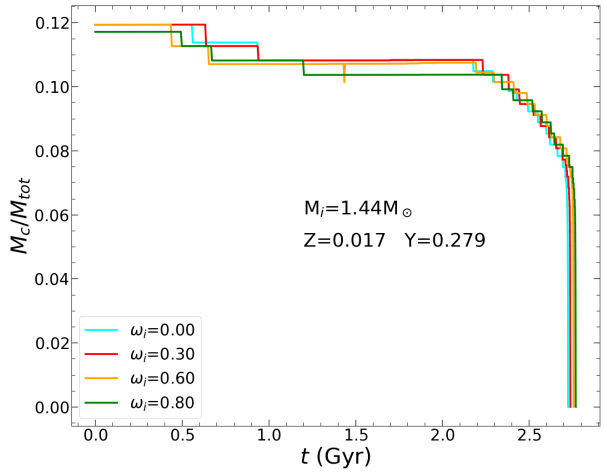

Fig. 4. Time evolution of the mass of the convective core (M_c/M_{tot}) during the H-burning phase for the model of $M_i = 1.44\,M_\odot$ and $Z = 0.017$.

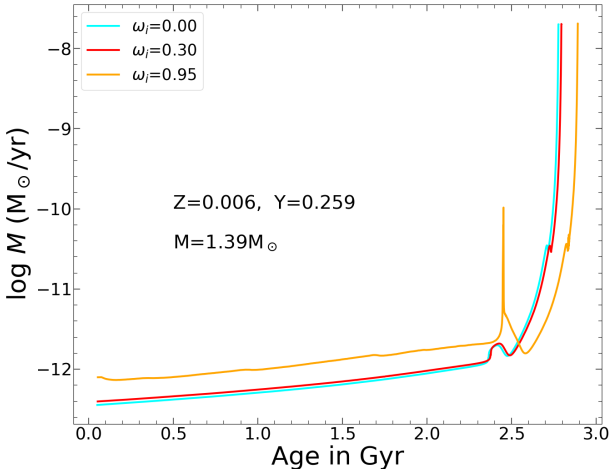

Fig. 6. Mass-loss rate as a function of time of star $M_i = 1.39\,M_\odot$, $Z = 0.006$ for three rotation rates, $\omega_i = 0.00$, 0.30, and 0.95 (cyan, red, and orange lines, respectively).

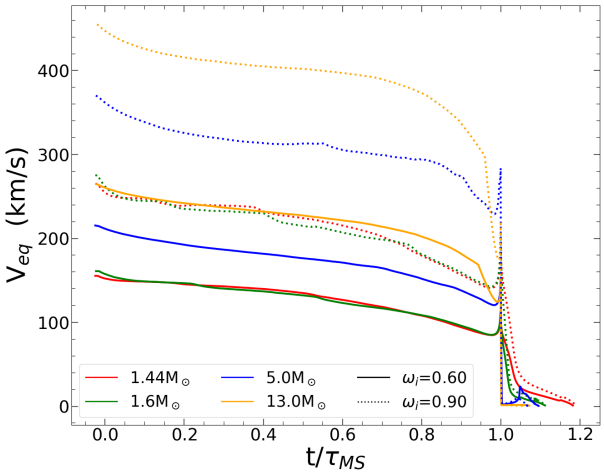

Fig. 5. Evolution of surface tangential velocity at the equator, V_{eq}, versus the time, t, scaled to the MS duration, τ_{MS}. The four selected mass models – 1.44 $M_\odot$ (red), 1.6 $M_\odot$ (green), 5 $M_\odot$ (blue), and 13 $M_\odot$ (orange) – are shown, with two initial rotation rates – $\omega_i = 0.60$ (solid line) and $\omega_i = 0.90$ (dotted line) – from the set with $Z = 0.014$, $Y = 0.273$.

this is due to the slightly heavier He-core mass discussed above. In general, we found that the TRGB luminosity of our models with $M \leq 1.5\,M_\odot$ is about $\log L/L_\odot \sim 3.385$–$3.420$, depending on the initial metallicity. This result is important in the context of the TRGB method of distance determinations, and the recent 'tension' in the values of the Hubble constant H_0 (see Freedman et al. 2019, 2020, and references therein for more details).

On the other hand, we also checked the effect of rotation on the mass-loss rate. Figure 6 shows the mass-loss rate of the 1.39 $M_\odot$ model with metallicity $Z = 0.006$, for three initial rotation rates, $\omega_i = 0.00$, 0.30 and 0.95. We plot $\log \dot{M}$ from the ZAMS to the end of the RGB. As expected from Eq. (7), during the MS phase the star with higher rotation rates has higher mass-loss rates. However, in the RGB phase, because of the decline of the surface rotational velocity, it evolves as a non-rotating star but with a slightly older age. In general, stars lose their mass at a rate of about $(0.6$–$6) \times 10^{-8}\,M_\odot$/yr at the TRGB stage. This result is based on the Reimers law that we adopted in our models. Interesting alternative models for mass loss have been proposed (Cranmer et al. 2007; Cranmer & Saar 2011), which will be the subject of other subsequent work. We note that during the stellar contraction phase just after the end of the MS, the tangential velocity may reach its critical value, at least for models with the highest initial rotation rates. This is the case for the model with $\omega_i = 0.95$ shown in Fig. 6. In this case, the mass loss as provided by Eq. (7), is enhanced by mechanical effects (Georgy et al. 2013; Costa et al. 2019b) as shown by the relative peak of about two orders of magnitude with respect to the other tracks, before entering the RGB phase.

Concerning the total mass lost on the RGB, we find that it is higher for the smaller initial masses. For non-rotating models of $Z = 0.004$, the stars with initial masses $M_i = 0.9\,M_\odot$, $1.16\,M_\odot$, and $1.36\,M_\odot$ lose about 11%, 6% and 4% of their initial mass, respectively. The total mass lost by the stars at the TRGB is illustrated in Fig. 7 for all six sets of metallicity and for two initial rotation rates, $\omega_i = 0.00$ and 0.95 (the solid- and dashed-lines, respectively). From this figure we also see that the key role in the total mass lost by the stars is taken, in decreasing order, by mass, metallicity, and rotation.

Figure 8 shows the difference in He-core mass at the TRGB between rotating models and their non-rotating counterparts, for three values of $\omega_i = 0.30, 0.60, 0.95$ and for six metallicities. The higher the initial rotation rate, the larger the He-core mass the star has at the tip, at any metallicity. While the surface rotation at this stage is small even for the largest ω_i, in the core it is still significant, as can be seen in Fig. 9. The larger the rotation, the less concentrated is the core, and a larger core mass is needed to reach the conditions for He ignition. At the larger initial masses, there is also a contribution of the more efficient rotational mixing during the MS phase. In general, the difference is $\leq 0.006\,M_\odot$, depending on ω_i. We note that these differences might affect the location of red clump stars in the HRD. This issue will be further investigated in a subsequent work.

3.2.2. From the ZAHB to the TP-AGB

Low-mass stars develop an electron-degenerate core and climb the RGB until they undergo the He flash. The latter requires large amounts of CPU times to be computed in detail (see Kippenhahn et al. 2012; Mocák et al. 2008, for more details).

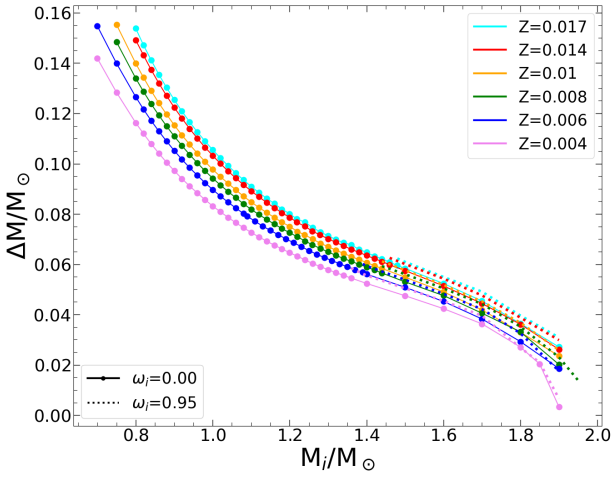

Fig. 7. Total mass lost until the TRGB versus initial mass for six different metallicity sets. Solid and dashed lines represent models with $\omega_{\rm i} = 0.00$ and $\omega_{\rm i} = 0.95$, respectively.

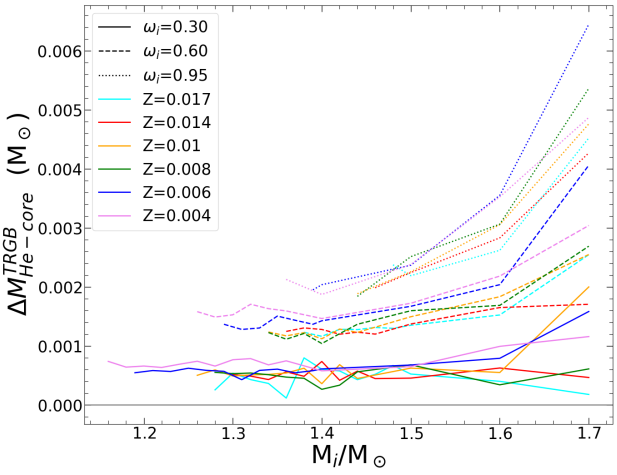

Fig. 8. Difference in He-core mass at the TRGB phase between the rotating models and their non-rotating counterparts, $\Delta M^{\rm TRGB}_{\rm He\text{-}core}$. Three initial rotating rates are considered: $\omega_{\rm i} = 0.30, 0.60, 0.95$ (solid, dashed, and dotted line, respectively). The colours represent different initial metallicities. The solid grey line marks the reference line for $\omega_{\rm i} = 0$ models.

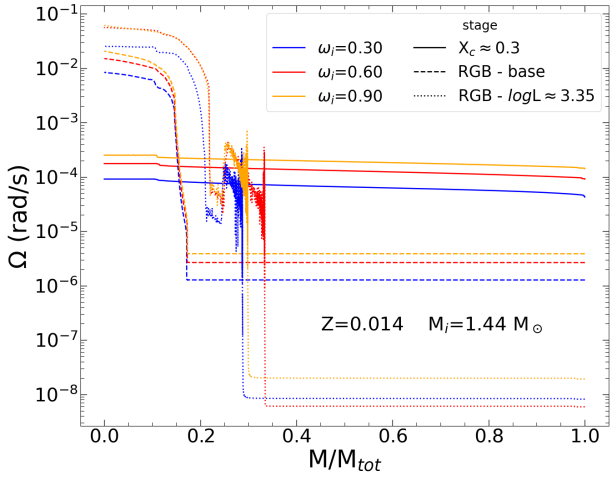

Fig. 9. Internal distribution of angular velocity, Ω. Three selected stages of models with $Z = 0.014$, $M_{\rm i} = 1.44\,M_\odot$ are presented: at which the central hydrogen $X_{\rm c} \approx 0.3$ during the MS (solid lines), at the base of the RGB phase (dashed lines), and near the TRGB with $\log L \approx 3.35$ (dotted lines). The colours represent different selected initial rotation models.

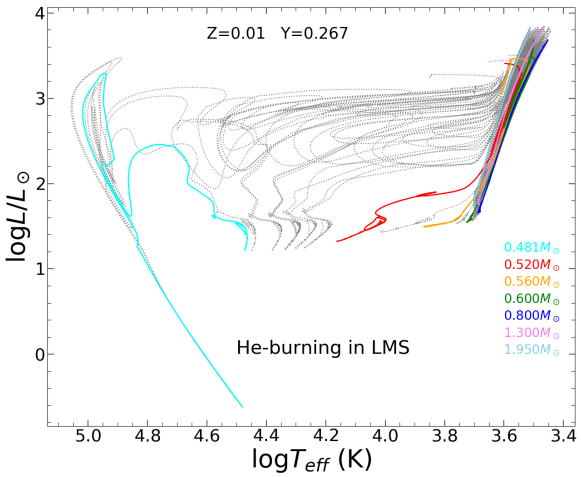

Fig. 10. He-burning phase of LMSs in the set with $Z = 0.01$, $Y = 0.267$. Tracks with ZAHB masses between 0.481 and 1.95 $M_\odot$ were computed in this case. A few of these tracks are marked with a different colour (with their mass in $M_\odot$ indicated in the legend) for reference.

Therefore, the computation of the evolutionary track is interrupted during the He flash, and restarted from a ZAHB model with the same He-core mass and surface chemical composition as the last RGB model. The initial ZAHB model is built following the method described in Bressan et al. (2012), taking into account the fraction of He that has been burned into carbon during the flash so that the degenerate core is lifted into a non-degenerate state. Then, the star is evolved along the horizontal branch and the evolution is terminated again after it experiences a few pulses of the TP-AGB phase. The evolutionary tracks in the HRD during the post-ZAHB phases of LMS are illustrated in Fig. 10, just for a single set of metallicity. Similar grids are available for all metallicities.

It is important to point out a few details in these calculations. First, rotation is turned off for the entire evolution beyond the ZAHB, simply because at those stages the rotational velocities have become small enough to not imply significant evolutionary effects.

Second, with respect to the previous version of PARSEC, the new tracks include mass loss starting from the ZAMS. Thus, for any given initial metallicity, we have different relations $M_{\rm TRGB}(M_{\rm i})$ for different $\omega_{\rm i}$. These relations are merged to obtain a complete unique sequence of $M_{\rm ZAHB}(M_{\rm i})$, with $M^i_{\rm ZAHB}$ spanning the range from the largest $M_{\rm TRGB}$ to the lowest value compatible with the thinnest envelope mass along the ZAHB sequence. We also pay attention to carefully sample the mass interval close to $M_{\rm HeF}$. We then interpolate on the sequence of non-rotating models to obtain a unique complete $M_{\rm core}(M^i_{\rm ZAHB})$ relation, which is used to construct the ZAHB model sequence.

3.3. Intermediate-mass and massive stars

Intermediate-mass stars are defined as having masses larger than the $M_{\rm HeF}$ limit and smaller than the $M_{\rm up}$ threshold for C ignition in the core. Both limits depend on the initial metallicity and the

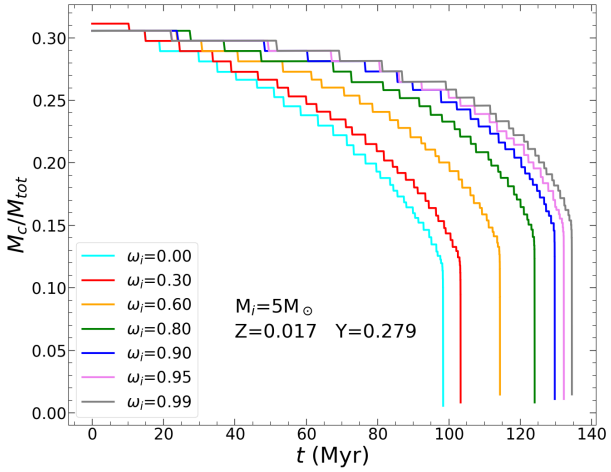

Fig. 11. Evolution of the mass of the convective core (M_c/M_{tot}) during the H-burning phase for the model of $M_i = 5.0\,M_\odot$ and $Z = 0.017$.

rotation rate. Massive stars are computed up to 14 $M_\odot$, leaving more massive stars to a dedicated paper, which is in preparation. Models with initial masses between M_{HeF} and 2.2 $M_\odot$ are computed with a mass step $\Delta M_i = 0.05\,M_\odot$; from 2.2 $M_\odot$ up to 6 $M_\odot$, $\Delta M_i = 0.2\,M_\odot$; up to 10 $M_\odot$, $\Delta M_i = 0.5\,M_\odot$ and $\Delta M_i = 1\,M_\odot$ above $M_i = 10\,M_\odot$. All these tracks start on the PMS phase and are interrupted either after the first few thermal pulses along the AGB or after the ignition of carbon in the core. All evolutionary tracks in this mass range have been computed with the maximum overshooting efficiency, (i.e. with $\lambda_{ov} = 0.4$ and $\Lambda_e = 0.7\,H_P$) and for all initial rotation rates from $\omega_i = 0.00$ to 0.99 (Sect. 2.4). The mass-loss rates of rotating stars follow the description in Sect. 2.6, while the formulation of de Jager et al. (1988) was adopted for non-rotating models.

In Fig. 2 we have already compared the evolution of a 5 $M_\odot$ model calculated with three different rotation rates, $\omega_i = 0.0$, 0.30, 0.90, with that of a 1.44 $M_\odot$ model with the same ω_i. Rotation impacts the evolution of IMSs in a way different from the LMSs. At the beginning of the evolution, only the geometrical effects of rotation are visible: in both cases, the models that rotate faster are less luminous and cooler. As evolution proceeds, IMSs develop a convective core surrounded by a radiative envelope where the meridional circulation works efficiently. As a result, rotational mixing provides more fresh fuel to the central core, and hence a more massive core is built up (see Fig. 11). This causes the IMSs models that rotate faster to become more luminous and to increase their MS lifetimes significantly (as shown in Fig. 3). Due to the larger core masses, the higher luminosity is maintained during all post-MS evolutionary phases. In contrast, in low-mass models even in the case with the largest rotation rate, the growth of the core is never so high to make it more luminous than the non-rotating one. At lower masses, rotation affects the effective temperature more than the luminosity.

Another consequence of rotational mixing during the MS phase is the transport of nuclear-burned products from the central region to the surface. This effect does not occur in non-rotating stars, until dredge-up events occur when the stars become red giants. In rotating stars, instead, significant mixing can occur at much earlier stages. The most evident effect of this mixing is an enhancement in the surface nitrogen and helium, followed by a depletion of both oxygen and carbon. Figure 12 shows the evolution of He, C, N, O abundance, luminosity, effective temperature, and ω, in three stars of mass 3 $M_\odot$, 5 $M_\odot$, and

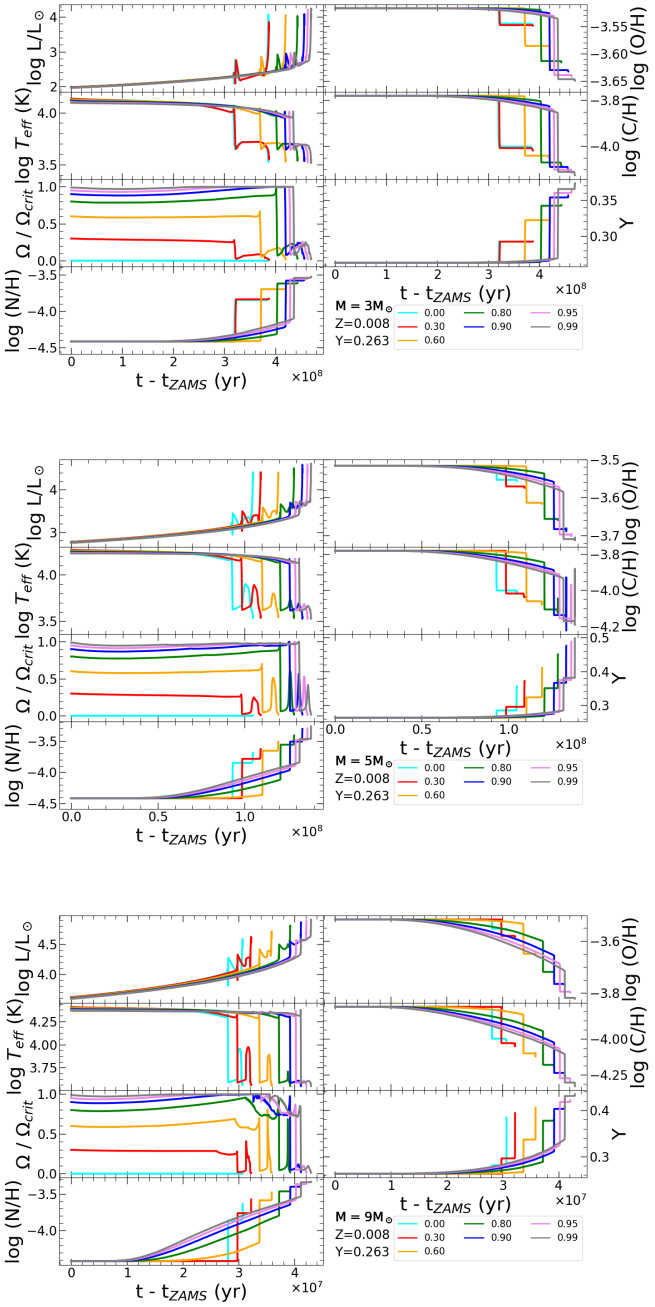

Fig. 12. Evolution of $\log L$, $\log T_{eff}$, rotation rate, ω, and surface abundances of N, C, O, and He at the surface for many initial rotation rates from $\omega_i = 0.00$ to 0.99 (from cyan to grey colours, respectively), for the cases of 3, 5, and 9 $M_\odot$ stars (in the three sets of panels from top to bottom, respectively) with $Z = 0.008$, $Y = 0.263$. The abundances of N, O, and C are by number and relative to the hydrogen abundance. For He, instead, we present the surface mass fraction Y.

9 $M_\odot$, for several initial rotation rates. The faster the star rotates on the MS, the more N and He appear at the surface, and the more C and O are depleted. The increase (decrease) in surface abundances develops gradually during the MS but suddenly jumps up (down) during the first dredge-up event that occurs after the end of the MS, when the star becomes a red giant. Afterwards, rotational mixing is no longer efficient, and the surface abundances remain constant until, eventually, the advent of the second dredge-up, which affects higher-mass IMSs, after the core-helium burning phase.

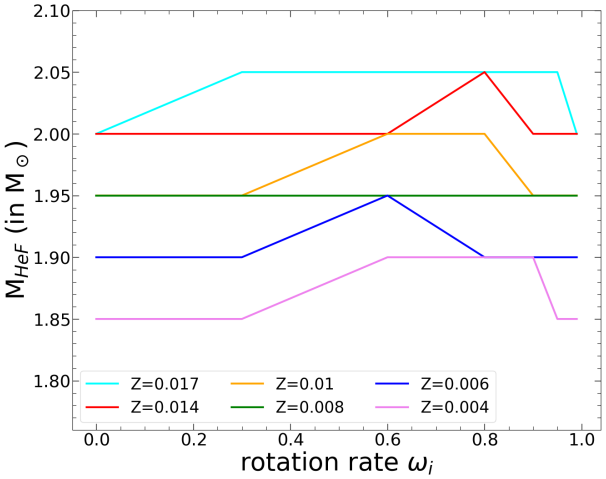

Fig. 13. Maximum mass at which the star burns He in the central region under a strongly degenerative condition, $M_{\rm HeF}$, versus the initial rotation rates. The colour refers to six computed metallicities in this paper, as indicated in the legend.

As can be seen in Figs. 2 and 12, the increased rotation rates on the MS also reduce the extension (in $T_{\rm eff}$) of the blue loop during the central He-burning phase. This is also an effect of the enhanced mixing caused by rotation (see the discussion of Costa et al. 2019b, and references therein).

The transition between LMSs and IMSs is set at a mass $M_{\rm HeF}$, above which He ignition takes place quietly in a non-degenerate core. Figure 13 shows the value of $M_{\rm HeF}$ as a function of initial rotation rates for the six metallicities computed in this paper. The plot has a resolution of 0.05 $M_\odot$, which is the mass separation between successive tracks computed around this mass range. First, lines of different colours illustrate the well-known dependence of $M_{\rm HeF}$ on the initial metallicity. Second, the dependence of $M_{\rm HeF}$ on initial rotation rate. For instance, the $Z = 0.004$ models have $M_{\rm HeF}$ values of either 1.85 $M_\odot$ or 1.90 $M_\odot$, while those with $Z = 0.017$ the values of 2.00 or 2.05 $M_\odot$. We find that at increasing rotation rates, the value of $M_{\rm HeF}$ also tends to increase with respect to the non-rotating models. However, when the initial rotation rate increases to values close to the critical breakup velocity, $M_{\rm HeF}$ declines again, returning to the value of non-rotating stars. This behaviour of $M_{\rm HeF}$ cannot be discussed in much detail because all changes occur within the mass separation step of 0.05 $M_\odot$. However, it is remarkable that rotation appears to have a limited impact on $M_{\rm HeF}$.

3.4. Comparison with PARSEC v1.2s and other databases

In Fig. 14 we show a comparison between the selected tracks calculated with the new version of the code, PARSEC v2.0, hereafter PS2, and with the older version, v1.2s, hereafter PS1. In both versions, we use the same initial chemical composition. In the leftmost panel, we show the case of a LMS with $M_{\rm i} = 0.8\,M_\odot$. Since this star does not possess a convective core during the H-burning phase, the HRD is the same for the two versions.

Instead, we recall that during the RGB evolution in the older version, PS1, overshooting at the bottom of the convective envelope has not been considered in the mass range ($\leq M_{\rm O1}$), producing RGBBs that were too luminous with respect to the observed ones (Fu et al. 2018). To cope with this evident discrepancy, in the new version PS2, we include EOV in LMSs as described in Sects. 2.2 and 2.3. The effect of adding an extra mixing at the bottom of the convective envelope is highlighted in the inset of the left panel in Fig. 14, where the RGBBs of stars with masses $0.8\,M_\odot \leq M_{\rm i} \leq 1.4\,M_\odot$, are shown.

However, in the mass range where stars develop a convective core in the MS (as in the case of $M_{\rm i} = 1.4\,M_\odot$), COV and EOV are fully considered in both versions of the PARSEC code. In PS2, we adopt a smaller value of the maximum COV parameter $\lambda_{\rm ov,max} = 0.4$, instead of the $\lambda_{\rm ov,max} = 0.5$ in PS1. Furthermore, in PS2 we adopt a diffusive treatment for convective mixing, where the diffusion equations are coupled with the nuclear reaction rates for all elements in the turbulent regions. In the PS1 version, the convective zones are 'instantaneously' homogenised at every time step. These differences already affect the MS phase of stars with convective cores (with $M_{\rm i} > M_{\rm O1}$), as shown in the middle panel in Fig. 14. The PS2 track with 1.4 $M_\odot$ presents a hotter and slightly fainter MS phase, and a fainter sub-giant phase.

On the other hand, the RGB phase has the same slope in both versions of PARSEC tracks. The new tracks show a brighter and cooler TRGB. These differences in the TRGB are caused by the more massive He-core and the more extended envelope at the tip. This is mainly due to the different overshoot parameters used in PS2 and the fact that in this new calculation mass loss was implemented along the evolution while, in PS1, models were evolved at constant mass, and mass loss was applied at the stage of isochrone calculation only.

In Fig. 15 we compare the luminosity at the TRGB of the PS2 models with that of PS1, Bag of Stellar Tracks and Isochrones (BaSTI; Hidalgo et al. 2018), and MESA Isochrones and Stellar Tracks (MIST; Choi et al. 2016) evolutionary tracks. The latter two databases also include convective overshooting and diffusion in their models. We can see that PS2 predicts a quite constant TRGB luminosity and, generally, above the luminosity of other models shown in the plot. The difference between the new and old versions of PARSEC is about ~0.01−0.02 dex. BaSTI gives an increased trend of TRGB luminosity with initial masses, which is in contrast with the trend from MIST. The PS2 TRGBs are ~0.04 dex brighter than MIST.

The right-hand panel of Fig. 14 shows the comparison between non-rotating models of IMSs of the two PARSEC code versions. In this case, the impact of the COV parameter is clear. The difference between PS1 and PS2's tracks starts from the MS and continues up to the He-burning phase. In particular, the new tracks are less luminous than the previous ones, due to their smaller $\lambda_{\rm ov,max}$ value.

Recently, Amard et al. (2019) published grids of STAREVOL models in which rotation is included for masses from 0.2 $M_\odot$ to 1.5 $M_\odot$. STAREVOL tracks are provided for three values of initial rotation rates, $\omega_{\rm i} = 0.20$, 0.40 and 0.60, while in this work we provide $\omega_{\rm i} = 0.30$, 0.60, 0.80, 0.90, 0.95, 0.99. To facilitate the comparison, we perform a few PARSEC v2.0 calculations with exactly the same initial composition ($Z = 0.0134$ and $Y = 0.269$) and the same initial rotation rate as STAREVOL. Figure 16 compares the models of 1.3 $M_\odot$ and 1.5 $M_\odot$ produced by both PARSEC v2.0 (red line) and STAREVOL (green line). The differences between our and STAREVOL models are significant. First, the STAREVOL tracks evolve until the end of the MS phase, while our tracks extend up to the He flash. Second, for the same initial mass, rotation rate, and composition, our MS stars are hotter and brighter. This might be explained by the many differences in the input physical parameters between the two codes. For example, Amard et al. (2019) do not include overshooting in their calculations, while we consider it for both the convective core

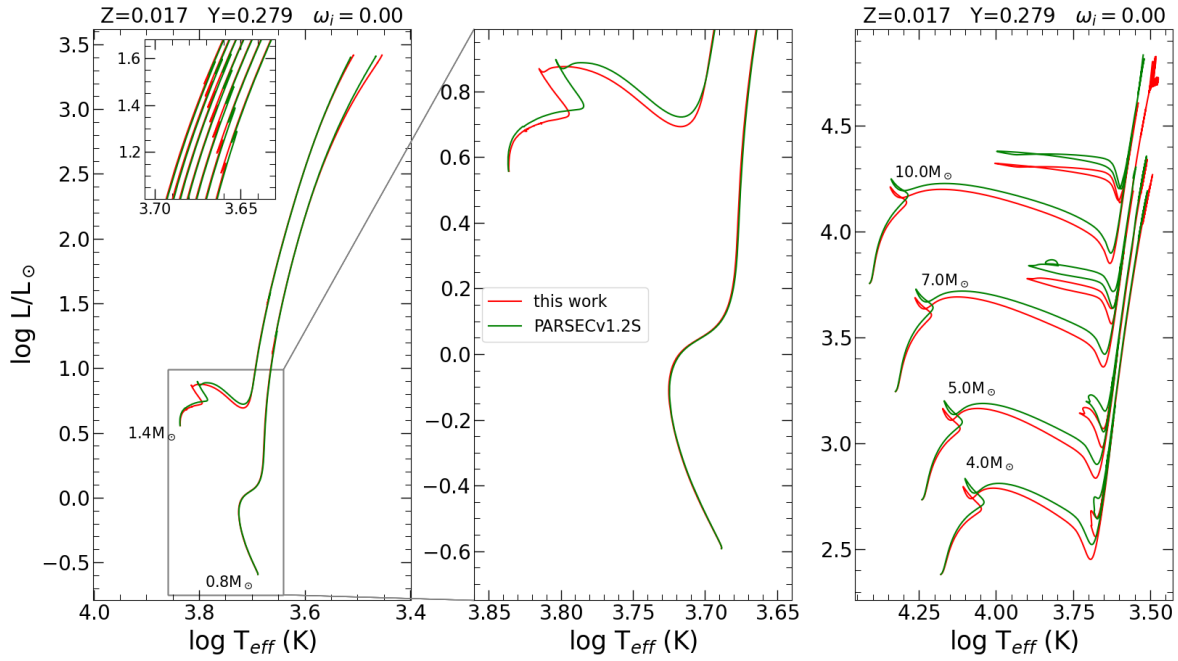

Fig. 14. HRD comparing tracks between PARSEC V2.0 (this work, red lines) and the previous version (PARSEC V1.2S, green lines) for non-rotating stars of $Z = 0.017$ and $Y = 0.279$. *Left-hand panel*: HRD of two LMSs with 0.8 and 1.4 $M_\odot$. Their PMS phase is not shown, because it is essentially the same in the two versions. The inset details the region around the RGBB for tracks in the mass range 0.8−1.4 $M_\odot$ with a step of 0.1 $M_\odot$. *Middle panel*: zooms into the MS regions of the 0.8 and 1.4 $M_\odot$ tracks. *Right panel*: instead compares intermediate-mass models for four different masses, as indicated.

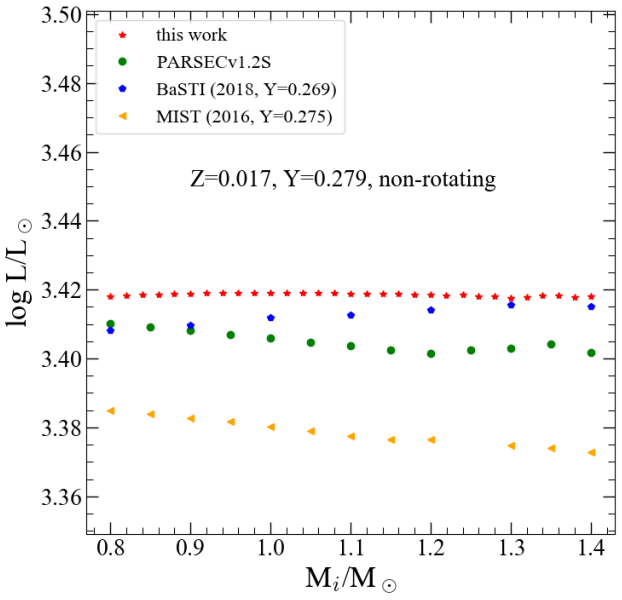

Fig. 15. Luminosity at the TRGB as a function of initial mass for the tracks produced in this work (with $\omega_i = 0$; red stars), in parsec v1.2S (green circles), and BaSTI (blue pentagons). The BaSTI tracks for a solar-scaled composition are taken from Hidalgo et al. (2018) with $Z = 0.01721$, $Y = 0.2695$.

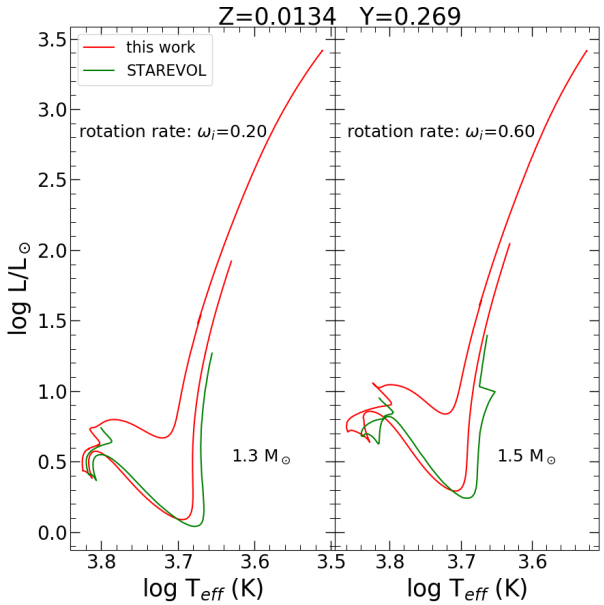

Fig. 16. Comparison on HRD of rotating tracks between this work (red lines) and STAREVOL (green lines) with the same $Z = 0.0134$ and $Y = 0.269$. *Left-hand panel*: slow-rotating tracks with a $\omega_i = 0.20$ and 1.3 $M_\odot$ star. *Right-hand panel*: same as the *left panel* but with $\omega_i = 0.60$ and $M_i = 1.5\ M_\odot$.

and the envelope. Third, there are differences in the implementation of rotation in each codes, namely, STAREVOL implements rotation from the PMS while we assign the rotation (and let it evolve) just before the ZAMS. It is also worth mentioning that there are other differences between the two codes; for example, they adopt the mixing-length parameter $\alpha_{\rm MLT} = 1.973$ and the nuclear reaction rates from the NACRE II database (Xu et al. 2013).

However, despite the differences listed above, the two codes give similar ages at the terminal-age-MS (TAMS). For instance, for the 1.3 $M_\odot$ star with $\omega_i = 0.2$ PS2 gives 3.74 Gyr while STAREVOL gives 3.94 Gyr.

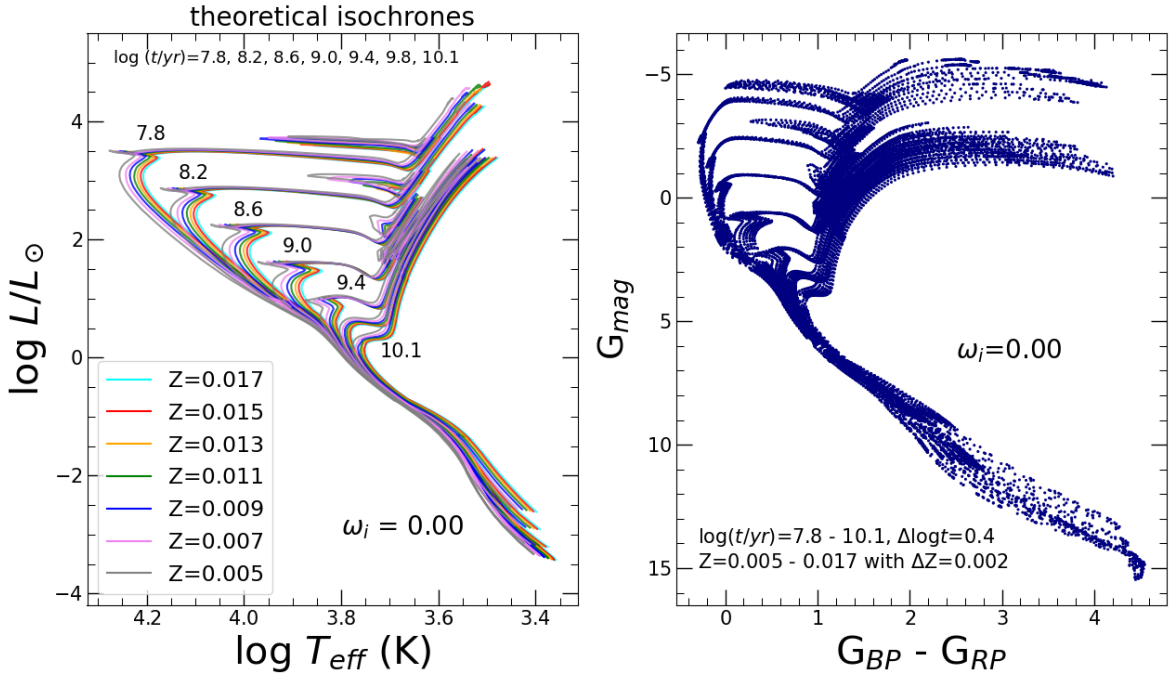

Fig. 17. Theoretical isochrones calculated with the TRILEGAL code. *Left-hand panel*: isochrones of non-rotating models for the ages $\log(t/\mathrm{yr}) = 7.8, 8.2, 8.6, 9.0, 9.4, 9.8, 10.1$ and seven different metallicities from 0.005 to 0.017 are shown in different colours, from grey to cyan, as indicated in the legend. *Right-hand panel*: corresponding CMD in *Gaia* passbands of the theoretical isochrones shown in the *left panel*.

Another similarity is in the mass-loss rates: at the TAMS, the $1.5\,M_\odot$ star with $\omega_\mathrm{i} = 0.6$ loses its mass with a rate of $\log \dot{M} = -11.70$ ($M_\odot$/yr) in PS2 while STAREVOL gives $\log \dot{M} = -11.62$ ($M_\odot$/yr), even though the codes use different schemes for the mass-loss rate. In particular, we use the enhanced formula from the Reimers law with $\eta = 0.2$ for rotating stars while STAREVOL uses the recipe of Cranmer & Saar (2011). However, we should note that at these early stages, the mass loss does not play a crucial role yet.

4. Isochrones

For all sets of evolutionary tracks described in the previous sections, we have constructed the corresponding isochrones. The initial phase begins from the PMS, and the final stage is either the beginning of the TP-AGB phase for low- and intermediate-mass models or the C-exhaustion for higher masses. As explained in Sect. 2.4, at a given initial metallicity and rotation rate, a certain number of low-mass models were not computed, due to our choice of decreasing ω_max at decreasing M_i, in the transition towards LMSs (Eq. (2)). While computing the isochrones, the missing tracks of a given ω_i are replaced by the track with the nearest initial mass in the set of tracks with the same metallicity and with ω_i immediately smaller. This ensures that the isochrones gradually shift from the required ω_i to the non-rotating case in the mass interval between M_{O2} and M_{O1}.

After selecting all the stellar tracks in each set, based on the initial metallicity and rotation rate, the computation of isochrones proceeds in the following steps: first, the computed stellar evolutionary tracks in each set are homogeneously divided into phases separated by a few characteristic 'equivalent evolutionary points'. Then, for a given age, the isochrone is constructed by interpolating all stellar properties between points of different initial mass but equivalent evolutionary stage. More details of the interpolation scheme can be found in Bertelli et al. (1990, 2008). In this paper, the isochrones are produced by a recent version of the TRILEGAL code (Girardi et al. 2005; Marigo et al. 2017), which interpolates all the additional quantities needed to characterise rotating stars. Several isochrones have been produced with metallicity in the range from 0.004 to 0.017 in steps of 0.001 and ages in the range from 10 Myr to ~13 Gyr at intervals of 0.05 in the scale log and for the seven sets of initial rotation rates from zero to $\omega_\mathrm{i} = 0.99$. As an example, the left-hand panel of Fig. 17 shows the theoretical isochrones of non-rotating stars for several ages and metallicities.

The theoretical isochrones provide the intrinsic properties of the stars, such as the luminosity, mean effective temperature, angular velocity, and radius at the pole and the equator. Then they are complemented with photometric magnitudes in several filters for comparison with observed CMDs. For non-rotating stars, this is usually done by using tables of bolometric corrections (BCs) as a function of effective temperature, surface gravity and metallicity (see Girardi et al. 2002); eventually these tables also consider the interstellar extinction in a star-to-star basis, as in Girardi et al. (2008). The right-hand panel of Fig. 17 shows non-rotating isochrones in the *Gaia* passbands, corresponding to those shown in the left-hand panel, where *Gaia* EDR3 photometry is adopted (see Riello et al. 2021).

Bolometric correction tables for rotating stars have at least two more parameters than those for non-rotating stars: the rotation rate ω and the inclination angle, i, of the line of sight with respect to the stellar rotation axes. Such BC tables are described in Girardi et al. (2019). They are already implemented in the YBC database[4] of BCs by Chen et al. (2019) and in the TRILEGAL code we use to produce the present isochrones. The left-hand panel of Fig. 18 shows some selected rotating isochrones. The two panels on the middle and right-hand side of Fig. 18 illustrate the result of applying the BCs to isochrones with rotation ω_i, and how the photometry changes when observing rotating stars

[4] http://stev.oapd.inaf.it/YBC/

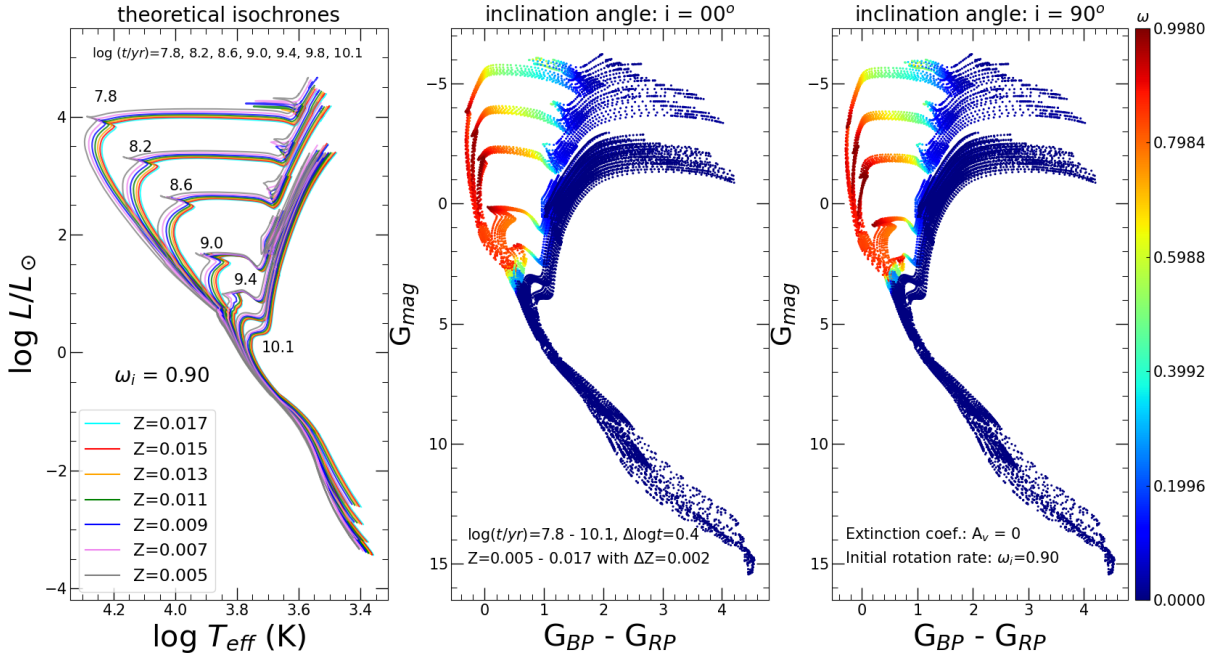

Fig. 18. Theoretical isochrones calculated with the TRILEGAL code. *Left-hand panel*: theoretical isochrones with the same parameter of $\log t$s and Zs as in Fig. 17 but for the $\omega_i = 0.90$ set. *Middle* and *right-hand panels*: corresponding CMD in the *Gaia*-passbands for two values of the inclination angle: $i = 0°$ (pole-on) and $i = 90°$ (equator-on). Changes in the rotation rate along the isochrones are indicated by the colour bar.

from $i = 0°$ (pole-on) and $i = 90°$ (equator-on). The changes in the photometry are the most remarkable for the stars close to the upper MS, since they are the stars that still retain a large fraction of their initial rotational velocity.

For cool red giants, the BC tables for rotating stars do not cover the complete range of low effective temperatures that might be necessary to build the isochrones containing fast-rotating stars. For instance, for $\omega = 0.9$ and $\log g = 2$ the BC tables defined in Girardi et al. (2019) are limited to effective temperatures above ~4000 K. Fortunately, inspection of our final isochrones reveals that this limitation is not a practical problem: it turns out that all giants with $T_{\rm eff}$ smaller than ~5000 K are slow rotators, with $\omega \lesssim 0.2$. Since these slow rotators have nearly spherical configurations, we decide to apply the BC tables for non-rotating stars from Chen et al. (2019) (YBC) to all stars with $T_{\rm eff} < 5250$ K, for all values of ω_i. This choice ensures a smooth behaviour of the colours, as can be appreciated in the middle and right panels of Fig. 18. To conclude this section, we note that the database of isochrones in several photometry systems is available online[5].

5. Discussion and conclusions

We have presented a new library of evolutionary tracks with rotation for LMSs and IMSs produced with PARSEC V2.0. Masses from 0.09 $M_\odot$ to 14 $M_\odot$ and metallicities between $Z = 0.004$ and $Z = 0.017$ are considered, for seven values of the initial rotation rate in the range $\omega_i = 0.00–0.99$. The major differences between the last version of PARSEC V2.0, and the previous one are: (i) the inclusion of rotation; (ii) the inclusion of mass loss along the evolution of all the stars because, for rotating models, it constitutes an important sink of angular momentum (Friend & Abbott 1986); and (iii) the treatment of turbulent mixing as a diffusive process together with rotational mixing, nuclear processing, and molecular diffusion (for LMSs). In particular, concerning the last point, we recall that, to estimate the efficiency of overshooting from the convective core, we were guided by the work of Costa et al. (2019a), where the maximum COV parameter was calibrated in a well-studied sample of eclipsing binary systems (Claret & Torres 2018), obtaining $\lambda_{\rm ov} = 0.4$.

We also calculated the isochrones up to the beginning of the TP-AGB phase or up to the end of the central C-burning phase. Using the TRILEGAL code, they can be interpolated in metallicity between $Z = 0.004$ and 0.017 and in the age range $7.0 \leq \log(t/{\rm yr}) \leq 10.1$.

To illustrate some important consequences of the above differences, we show in Figs. 19 and 20 two preliminary fits to the observed CMD of the open clusters M67 and NGC 6633, respectively. M 67 (NGC 2682) is a well-known test bench for studying the internal physics of stellar models of LMSs with typical turnoff masses around 1.2 $M_\odot$. In particular, its CMD was used to calibrate the efficiency of convective overshooting, due to the well-developed convective core in stars around its turnoff region. Furthermore, the cluster, together with other known open clusters, was also used to obtain the age-metallicity relation for the Milky Way disc stars (e.g. Viscasillas Vázquez et al. 2022). Its age has been repeatedly estimated over the years: Sarajedini et al. (2009) reported an age between 3.5 and 4.0 Gyr; from the asteroseismic properties of the giant and red clump stars, Stello et al. (2016) derived an age of the cluster of 3.46 ± 0.13 Gyr; more recently, using the data from the *Gaia* Second Data Release (hereafter GDR2), Bossini et al. (2019) derived a distance modulus $(m - M)_0 = 9.726$ mag, an interstellar extinction coefficient $A_V = 0.115$ mag, and an age of 3.639 ± 0.017 Gyr (see Arenou et al. 2018; Gaia Collaboration 2018a,b; Lindegren et al. 2018, for more details about GDR2).

The M 67 CMD, shown in Fig. 19, was obtained from the data provided by Cantat-Gaudin et al. (2018), who determined photometry, memberships, mean distances, and proper motions of stars in 1229 open clusters. It should be noted that the stars

[5] http://stev.oapd.inaf.it/cmd

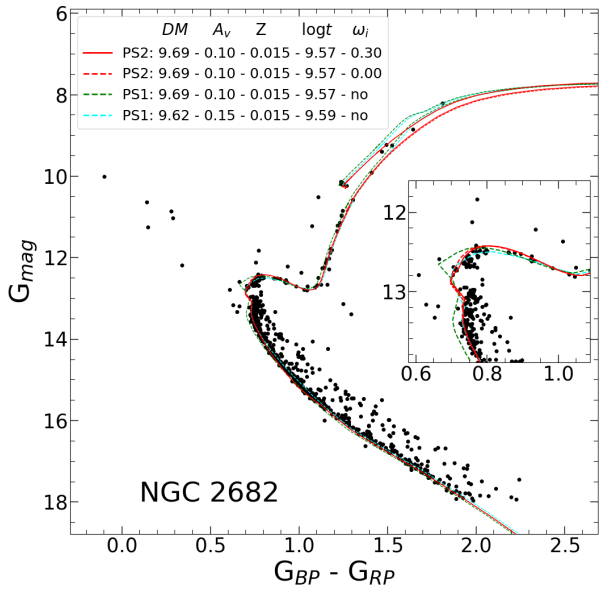

Fig. 19. CMD of open cluster M 67 (NGC 2682) from GDR2 data, overplotted with the isochrones that are produced in this work (solid and dashed red lines, labelled PS2) and those from the previous version, PARSEC V1.2S (dashed green and cyan lines, labelled PS1). The parameters of the isochrones, DM = $(m - M)_0$, A_V, Z, $\log t/\mathrm{yr}$ and ω_i, are displayed in the legend. The inset figure zooms into the turnoff region of this cluster.

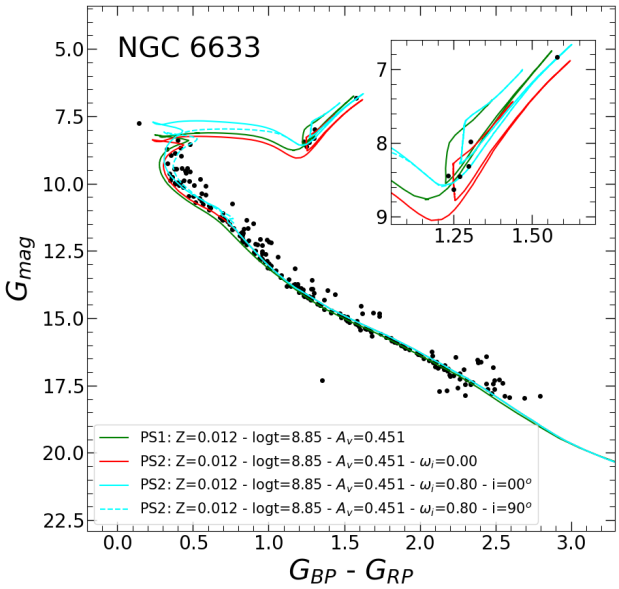

Fig. 20. CMD of the open cluster NGC 6633 from GDR2. The displayed isochrones are for metallicity $Z = 0.012$, $\log(t/\mathrm{yr}) = 8.85$, $(m - M)_0 = 7.841$, and $A_V = 0.451$ mag. The red line represents the non-rotating case, and the two cyan lines are for rotating isochrones with the same $\omega_i = 0.80$, and inclination angles $i = 0°$ (solid line) and $i = 90°$ (dashed line). The green line is the isochrone obtained with PARSEC V1.2S assuming the same parameters of the previous non-rotating case.

are limited to apparent $G \lesssim 18$ mag to keep the photometric precision in *Gaia*'s passbands at the level of a few millimag (see Godoy-Rivera et al. 2021; Bossini et al. 2019; Evans et al. 2018, for more details). Also plotted in Fig. 19 are a number of our isochrones selected with the following criteria. Lines labelled PS2 indicate our best-fit PARSEC V2.0 isochrones. The fit was obtained by adopting the distance modulus obtained by Bossini et al. (2019), $(m-M)_0 = 9.726$ mag, but correcting it for a zero-point offset of −30 μarcsec (Lindegren et al. 2018). The final corrected distance modulus is $(m - M)_0 = 9.69$ mag. For an initial composition of $Z = 0.015$ ([Fe/H] ∼ 0), $Y = 0.275$ (our corresponding He value), the best fit was obtained by adopting an extinction $A_V = 0.1$ mag and an age of $\log(t/\mathrm{yr}) = 9.57$. Plotted in the figure are both a non-rotating isochrone (dashed red line) and one for a slow rotation (solid red line). For both isochrones we use the same best-fit parameters because the adopted low rotation only marginally affects the region above the cluster turnoff.

In the same figure we also show the results we obtain using PARSEC V1.2S, labelled 'PS1'. For the model represented by the dashed green line, we adopt the same fit parameters as the PS2 solutions. The inset in the figure is a zoomed-in look at the turnoff region to highlight the differences between the isochrones. We see that this PARSEC V1.2S isochrone has a more pronounced hook at the same fitting parameters. This is an evident feature of models computed with a larger COV parameter. Instead, the dashed cyan isochrone was drawn to reproduce the fit obtained with PS1 models, keeping only the metallicity fixed and letting the other parameters vary within reasonable uncertainties. For this second PS1 model, which runs almost on top of the PS2 isochrones, we adopted a slightly shorter distance modulus, $(m - M)_0 = 9.62$, a larger extinction, $A_V = 0.15$ mag, and a 5% older age, $\log(t/\mathrm{yr}) = 9.59$. We note that all four isochrones run almost superimposed onto one another in the sub-giant branch, which, being an almost horizontal feature in the CMD, is a robust indicator of the apparent distance. The new fitting parameters result from the need to diminish the hook extension that, with PARSEC V1.2S, can only be done by using a slightly older age for a fixed metallicity. The variation in the distance modulus and the attenuation almost compensate for each other, but the latter is also needed to improve the fitting of the colours of the turnoff region. The differences of the parameters between this fit and the PS2 ones should be representative of the differences obtained by using the new version of PARSEC instead of the previous V1.2S version in this age domain.

Recently, it has been shown that M 67 harbours an interesting spectroscopic binary system located near the turnoff region, WOCS 11028, that challenges theoretical models (see Sandquist et al. 2021, for a thorough discussion). Briefly, the mass of the primary component is estimated to be $M_{\mathrm{WOCSa}} = 1.222 \pm 0.006\, M_\odot$, while current predictions using different stellar evolution codes (including PARSEC V1.2S) give values that are lower by $\delta m = 0.05\, M_\odot$ (i.e. about 8σ lower). We confirm that we also get the same result with the new version of PARSEC and leave this problem to a more exhaustive investigation using new PARSEC models with varying initial metallicity and He content (see also Sandquist et al. 2021).

Another object we present in this paper as a preliminary check of the new models is the young open cluster NGC 6633, also present in the GDR2 catalogue. High-resolution spectroscopy for NGC 6633 comes from the analysis by Casamiquela et al. (2021), who studied the age metallicity relation of the Milky Way using 47 open clusters observed with *Gaia*. Bossini et al. (2019) derived for NGC 6633 $(m - M)_0 = 7.866^{+0.024}_{-0.025}$ mag, $\log(t/\mathrm{yr}) = 8.888^{+0.006}_{-0.032}$, and $A_V = 0.451^{+0.025}_{-0.02}$ mag. With the same procedure used for M 67, we fitted the CMD of NGC 6633 with the new isochrones, adopting $Z = 0.012$, $Y = 0.270$, $A_V = 0.451$ mag, and distance modulus $(m - M)_0 = 7.841$ mag, including a −30μarcsec offset in

Gaia parallaxes, and the age of $\log(t/\mathrm{yr}) = 8.85$ (Fig. 20). Both non-rotating and rotating isochrones are displayed with values indicated in the corresponding labels. The lower MS is very well fitted, while the extended MS turnoff region is fully reproduced by rotating isochrones, also taking the effects of inclination angles in account, which, in this cluster, are clearly seen. Furthermore, the different rotational velocities in this cluster can also explain the particular feature visible near the red clump. Indeed, if only rotating models had been used, as needed by the fit of the turnoff region, it would have been difficult to explain the position of the three stars that clearly fall below the corresponding He clump, given the much shorter corresponding evolutionary lifetimes. They are instead fully compatible with the He clump of non-rotating models of similar age. Thus, even in NGC 6633 there are hints for the presence of at least one population of non-rotating stars and another of fast rotators, as in the case of the young LMC cluster NGC 1866 (Costa et al. 2019b).

Acknowledgements. G.C. acknowledges financial support from the European Research Council for the ERC Consolidator grant DEMOBLACK, under contract no. 770017. L.G. and P.M. acknowledge financial support from Padova University, Department of Physics and Astronomy Research Project 2021 (PRD 2021). A.B. acknowledges funding from PRIN MIUR 2017 prot. 20173ML3WW 001 and 002, 'Opening the ALMA window on the cosmic evolution of gas, stars and supermassive black holes'. C.Y. and X.F. acknowledge the science research grants from the China Manned Space Project with NO. CMS-CSST-2021-A08. Y.C. acknowledges the financial support from the National Natural Science Foundation of China (12003001) and the National Key R&D Program of China (2021YFC2203100). X.F. thanks the support of China Postdoctoral Science Foundation No. 2020M670023, the National Key R&D Program of China No. 2019YFA0405500 and the National Natural Science Foundation of China (NSFC) under grant No. 11973001, 12090040, and 12090044. P.G. acknowledges support provided by NASA through grant HST-AR-15023 from the Space Telescope Science Institute, which is operated by the Association of Universities for Research in Astronomy, Inc., under NASA contract NAS5-26555.

References

Aaronson, M., & Mould, J. 1982, ApJS, 48, 161
Allard, F., Homeier, D., & Freytag, B. 2012, Phil. Trans. R. Soc. London Ser. A, 370, 2765
Alongi, M., Bertelli, G., Bressan, A., & Chiosi, C. 1991, A&A, 244, 95
Amard, L., Palacios, A., Charbonnel, C., et al. 2019, A&A, 631, A77
Aparicio, A., Bertelli, G., Chiosi, C., & Garcia-Pelayo, J. M. 1990, A&A, 240, 262
Arenou, F., Luri, X., Babusiaux, C., et al. 2018, A&A, 616, A17
Asplund, M., Grevesse, N., & Jacques Sauval, A. 2006, Nucl. Phys. A, 777, 1
Asplund, M., Grevesse, N., Sauval, A. J., & Scott, P. 2009, ARA&A, 47, 481
Bertelli, G., Bressan, A. G., & Chiosi, C. 1984, A&A, 130, 279
Bertelli, G., Bressan, A., Chiosi, C., & Angerer, K. 1986, A&AS, 66, 191
Bertelli, G., Betto, R., Bressan, A., et al. 1990, A&AS, 85, 845
Bertelli, G., Girardi, L., Marigo, P., & Nasi, E. 2008, A&A, 484, 815
Bjorkman, J. E., & Cassinelli, J. P. 1993, ApJ, 409, 429
Bloecker, T. 1995, A&A, 297, 727
Böhm, K. H. 1958, ZAp, 46, 245
Böhm-Vitense, E. 1958, ZAp, 46, 108
Bossini, D., Miglio, A., Salaris, M., et al. 2015, MNRAS, 453, 2290
Bossini, D., Vallenari, A., Bragaglia, A., et al. 2019, A&A, 623, A108
Bressan, A. G., Chiosi, C., & Bertelli, G. 1981, A&A, 102, 25
Bressan, A., Bertelli, G., & Chiosi, C. 1986, Mem. Soc. Astron. It., 57, 411
Bressan, A., Fagotto, F., Bertelli, G., & Chiosi, C. 1993, A&AS, 100, 647
Bressan, A., Marigo, P., Girardi, L., et al. 2012, MNRAS, 427, 127
Caffau, E., Ludwig, H. G., Steffen, M., Freytag, B., & Bonifacio, P. 2011, Sol. Phys., 268, 255
Cantat-Gaudin, T., Jordi, C., Vallenari, A., et al. 2018, A&A, 618, A93
Casamiquela, L., Soubiran, C., Jofré, P., et al. 2021, A&A, 652, A25
Cassisi, S., Salaris, M., & Bono, G. 2002, ApJ, 565, 1231
Catalán, S., Isern, J., García-Berro, E., & Ribas, I. 2008, MNRAS, 387, 1693
Chaboyer, B., & Zahn, J. P. 1992, A&A, 253, 173
Chen, Y., Girardi, L., Bressan, A., et al. 2014, MNRAS, 444, 2525
Chen, Y., Bressan, A., Girardi, L., et al. 2015, MNRAS, 452, 1068
Chen, Y., Girardi, L., Fu, X., et al. 2019, A&A, 632, A105
Chieffi, A., & Limongi, M. 2013, ApJ, 764, 21
Chieffi, A., & Limongi, M. 2017, ApJ, 836, 79
Choi, J., Dotter, A., Conroy, C., et al. 2016, ApJ, 823, 102
Christensen-Dalsgaard, J., Monteiro, M. J. P. F. G., Rempel, M., & Thompson, M. J. 2011, MNRAS, 414, 1158
Claret, A., & Torres, G. 2016, A&A, 592, A15
Claret, A., & Torres, G. 2017, ApJ, 849, 18
Claret, A., & Torres, G. 2018, ApJ, 859, 100
Claret, A., & Torres, G. 2019, ApJ, 876, 134
Costa, G., Girardi, L., Bressan, A., et al. 2019a, MNRAS, 485, 4641
Costa, G., Girardi, L., Bressan, A., et al. 2019b, A&A, 631, A128
Costa, G., Bressan, A., Mapelli, M., et al. 2021, MNRAS, 501, 4514
Costa, G., Ballone, A., Mapelli, M., & Bressan, A. 2022, MNRAS, 516, 1072
Cranmer, S. R., & Saar, S. H. 2011, ApJ, 741, 54
Cranmer, S. R., van Ballegooijen, A. A., & Edgar, R. J. 2007, ApJS, 171, 520
D'Antona, F., Milone, A. P., Tailo, M., et al. 2017, Nat. Astron., 1, 0186
de Jager, C., Nieuwenhuijzen, H., & van der Hucht, K. A. 1988, A&AS, 72, 259
Demarque, P., Woo, J.-H., Kim, Y.-C., & Yi, S. K. 2004, ApJS, 155, 667
Dupree, A. K., Dotter, A., Johnson, C. I., et al. 2017, ApJ, 846, L1
Eggenberger, P., Miglio, A., Montalban, J., et al. 2010, A&A, 509, A72
Ekström, S., Georgy, C., Eggenberger, P., et al. 2012, A&A, 537, A146
Espinosa Lara, F., & Rieutord, M. 2007, A&A, 470, 1013
Evans, D. W., Riello, M., De Angeli, F., et al. 2018, A&A, 616, A4
Fagotto, F., Bressan, A., Bertelli, G., & Chiosi, C. 1994a, A&AS, 104, 365
Fagotto, F., Bressan, A., Bertelli, G., & Chiosi, C. 1994b, A&AS, 105, 29
Freedman, W. L., Madore, B. F., Hatt, D., et al. 2019, ApJ, 882, 34
Freedman, W. L., Madore, B. F., Hoyt, T., et al. 2020, ApJ, 891, 57
Friend, D. B., & Abbott, D. C. 1986, ApJ, 311, 701
Fu, X., Bressan, A., Marigo, P., et al. 2018, MNRAS, 476, 496
Gaia Collaboration (Babusiaux, C., et al.) 2018a, A&A, 616, A10
Gaia Collaboration (Brown, A. G. A., et al.) 2018b, A&A, 616, A1
Georgy, C., Ekström, S., Eggenberger, P., et al. 2013, A&A, 558, A103
Girardi, L., Bressan, A., Bertelli, G., & Chiosi, C. 2000, A&AS, 141, 371
Girardi, L., Bertelli, G., Bressan, A., et al. 2002, A&A, 391, 195
Girardi, L., Groenewegen, M. A. T., Hatziminaoglou, E., & da Costa, L. 2005, A&A, 436, 895
Girardi, L., Dalcanton, J., Williams, B., et al. 2008, PASP, 120, 583
Girardi, L., Costa, G., Chen, Y., et al. 2019, MNRAS, 488, 696
Godoy-Rivera, D., Pinsonneault, M. H., & Rebull, L. M. 2021, ApJS, 257, 46
Grevesse, N., & Sauval, A. J. 1998, Space Sci. Rev., 85, 161
Heger, A., Langer, N., & Woosley, S. E. 2000, ApJ, 528, 368
Hidalgo, S. L., Pietrinferni, A., Cassisi, S., et al. 2018, ApJ, 856, 125
Higl, J., Müller, E., & Weiss, A. 2021, A&A, 646, A133
Iglesias, C. A., & Rogers, F. J. 1996, ApJ, 464, 943
Itoh, N., Uchida, S., Sakamoto, Y., Kohyama, Y., & Nozawa, S. 2008, ApJ, 677, 495
Jermyn, A. S., Tout, C. A., & Chitre, S. M. 2018, MNRAS, 480, 5427
Kalirai, J. S., Hansen, B. M. S., Kelson, D. D., et al. 2008, ApJ, 676, 594
Kippenhahn, R., & Thomas, H. C. 1970, in IAU Colloq. 4: Stellar Rotation, ed. A. Slettebak, 20
Kippenhahn, R., Meyer-Hofmeister, E., & Thomas, H. C. 1970, A&A, 5, 155
Kippenhahn, R., Weigert, A., & Weiss, A. 2012, Stellar Structure and Evolution (Berlin, Heidelberg: Springer)
Komatsu, E., Smith, K. M., Dunkley, J., et al. 2011, ApJS, 192, 18
Lindegren, L., Hernández, J., Bombrun, A., et al. 2018, A&A, 616, A2
Lodders, K., Palme, H., & Gail, H. P. 2009, Landolt Börnstein, 4B, 712
Maeder, A. 1975, A&A, 40, 303
Maeder, A. 2009, Physics, Formation and Evolution of Rotating Stars (Berlin, Heidelberg: Springer)
Maeder, A., & Meynet, G. 2000, A&A, 361, 159
Marigo, P., & Aringer, B. 2009, A&A, 508, 1539
Marigo, P., Bressan, A., Nanni, A., Girardi, L., & Pumo, M. L. 2013, MNRAS, 434, 488
Marigo, P., Girardi, L., Bressan, A., et al. 2017, ApJ, 835, 77
McQuillan, A., Mazeh, T., & Aigrain, S. 2014, ApJS, 211, 24
Meynet, G., & Maeder, A. 1997, A&A, 321, 465
Meynet, G., Maeder, A., Schaller, G., Schaerer, D., & Charbonnel, C. 1994, A&AS, 103, 97
Miglio, A., Brogaard, K., Stello, D., et al. 2012, MNRAS, 419, 2077
Mocák, M., Müller, E., Weiss, A., & Kifonidis, K. 2008, A&A, 490, 265
Mowlavi, N., Eggenberger, P., Meynet, G., et al. 2012, A&A, 541, A41
Noll, A., Deheuvels, S., & Ballot, J. 2021, A&A, 647, A187
Paxton, B., Bildsten, L., Dotter, A., et al. 2011, ApJS, 192, 3
Paxton, B., Schwab, J., Bauer, E. B., et al. 2018, ApJS, 234, 34
Pietrinferni, A., Cassisi, S., Salaris, M., & Castelli, F. 2004, ApJ, 612, 168
Pols, O. R., Schröder, K.-P., Hurley, J. R., Tout, C. A., & Eggleton, P. P. 1998, MNRAS, 298, 525

Potter, A. T., Tout, C. A., & Eldridge, J. J. 2012, MNRAS, 419, 748
Reimers, D. 1975, Mem. Soc. R. Sci. Liege, 8, 369
Reimers, D. 1977, A&A, 61, 217
Renzini, A., & Fusi Pecci, F. 1988, ARA&A, 26, 199
Riello, M., de Angeli, F., Evans, D. W., et al. 2021, VizieR Online Data Catalog: J/A+A/649/A3
Rosenfield, P., Marigo, P., Girardi, L., et al. 2014, ApJ, 790, 22
Roxburgh, I. W. 1978, A&A, 65, 281
Royer, F., Zorec, J., & Gómez, A. E. 2007, A&A, 463, 671
Salaris, M., Serenelli, A., Weiss, A., & Miller Bertolami, M. 2009, ApJ, 692, 1013
Sandquist, E. L., Latham, D. W., Mathieu, R. D., et al. 2021, AJ, 161, 59
Sarajedini, A., Dotter, A., & Kirkpatrick, A. 2009, ApJ, 698, 1872
Saslaw, W. C., & Schwarzschild, M. 1965, ApJ, 142, 1468
Schröder, K. P., & Cuntz, M. 2005, ApJ, 630, L73
Schwarzschild, M. 1958, Structure and Evolution of the Stars (Princeton: Princeton University Press)
Song, N., Alexeeva, S., Sitnova, T., et al. 2020, A&A, 635, A176
Sonoi, T., Ludwig, H. G., Dupret, M. A., et al. 2019, A&A, 621, A84
Spada, F., Demarque, P., Kim, Y. C., Boyajian, T. S., & Brewer, J. M. 2017, ApJ, 838, 161
Spera, M., Mapelli, M., Giacobbo, N., et al. 2019, MNRAS, 485, 889
Stello, D., Vanderburg, A., Casagrande, L., et al. 2016, ApJ, 832, 133
Talon, S., & Zahn, J. P. 1997, A&A, 317, 749
Tang, J., Bressan, A., Rosenfield, P., et al. 2014, MNRAS, 445, 4287
Torres, G., Vaz, L. P. R., Sandberg Lacy, C. H., & Claret, A. 2014, AJ, 147, 36
Ventura, P., Zeppieri, A., Mazzitelli, I., & D'Antona, F. 1998, A&A, 334, 953
Viani, L. S., Basu, S., Ong, J. M. J., Bonaca, A., & Chaplin, W. J. 2018, ApJ, 858, 28
Vink, J. S., de Koter, A., & Lamers, H. J. G. L. M. 2001, A&A, 369, 574
Viscasillas Vázquez, C., Magrini, L., Casali, G., et al. 2022, A&A, 660, A135
von Steiger, R., & Zurbuchen, T. H. 2016, ApJ, 816, 13
von Zeipel, H. 1924a, MNRAS, 84, 665
von Zeipel, H. 1924b, MNRAS, 84, 684
Weiss, A., & Schlattl, H. 2008, Ap&SS, 316, 99
Xu, Y., Goriely, S., Jorissen, A., Chen, G. L., & Arnould, M. 2013, A&A, 549, A106
Zahn, J. P. 1992, A&A, 265, 115